Spectra of a highly frustrated quantum spin ladder

Bachelor Thesis

Adriano Di Pietro

Chair of Theoretical Solid State Physics

Faculty of Physics

Ludwig-Maximilians-University Munich

Supervisors:

Prof. Dr. Jan von Delft and M. Sc. Benedikt Bruognolo

Munich, August 6, 2017

Anregungspektren einer hochfrustrierten Spin-Leiter

Bachelor Arbeit

Adriano Di Pietro

Lehrstuhl für theoretische Festkörperphysik

Fakultät für Physik

Ludwig-Maximilians-Universität München

Betreuer:

Prof. Dr. Jan von Delft und M. Sc. Benedikt Bruognolo

München, den 6. August 2017

Contents

1. Introduction

Ever since the pioneering work of Ernst Ising, low dimensional magnetic systems have attracted the attention of many researchers. Over the years, refinements in numerical techniques and the increase of computational resources have opened access to the characterization of this class of quantum many body systems. Although we are still restricted to the study of relatively simple systems, these already often reveal many unusual exotic physical phenomena such as quantum phase transitions [24]. Low-dimensional frustrated magnetic systems have been of particular interest for solid state theorists in recent years. This particular class of magnets feature extremely interesting low-energy properties such as the appearance of new phases of matter such as spin liquid- [19, pp. 23-27] and spin ice- [19, p. 239] phase.

In the following work, we will inspect the frustrated spin-1/2 ladder with cross couplings. This system is known to exhibit a quantum phase transition from a spin-singlet to spin-triplet phase [35]. Our goal will be to characterize the low energy excitation spectrum in the vicinity of thecritical point and observe the influence of finite temperatures on the spectral features. We will explore the interplay of frustration and thermal fluctuations will cause drastic spectral weight redistribution, especially as we approach criticality. In chapter 2, we will characterize frustrated systems and describe some of their peculiarities. In section 2.2 we will take a closer look at the frustrated spin ladder in order to develop a deeper understanding for the system we want to study. Chapter 3 will elaborate on the excitation spectrum of such a spin system and how it can be obtained in the contex of inelastic neutron scattering. Sections 3.15 ,3.4, 3.5 and 3.6 are devoted to introducing the numerical tools required for the theoretical calculation of the spectra. In the scope of this thesis we refrain from providing a complete discussion of these frameworks, we do however present some of their main ideas. The numerical techniques we discuss are density matrix renormalization group [31, 25] (both in the time dependent (tDMRG) and time independent variant (DMRG)) and mixed state purification. In order to understand how these methods work, we also provide a brief introduction into the matrix product state (MPS) and tensor network (TN) formalisms [22, 25]. Once the numerical background has been provided, we discuss our numerical results in Chapter 4 and draw some comparisons with the already known results presented in Refs. [15, 16]

2. Frustrated Magnetism

In the following, we will make some introductory remarks on frustrated systems necessary to understand many of the features of the spin ladder system.
After a more generic discussion on some of the exotic features connected to magnetic frustration, we will introduce the specific spin ladder model and provide the necessary background to interpret to numerical results which will be reported later on in the work.

2.1 Frustrated systems

Many-body frustrated systems are characterized by Hamiltonians that do not allow for the simultaneous minimization of all the interaction energies. These particular Hamiltonians can arise when we try to merge physical systems (such as Ising spin ensembles) on ordered structures such as Bravais lattices. If we define the exchange energy of two interacting spins as follows:

$$E = J(\vec{S}_i \cdot \vec{S}_j)\,, \tag{2.1}$$

we will have one of two cases:

- $J < 0$: ferromagnetic ordering.

- $J > 0$: antiferromagnetic ordering.

The most prominent example of frustration is represented by the the antiferromagnetic Heisenberg Hamiltonian applied on a 2-dimensional triangular lattice:

$$\hat{H} = J \sum_{<i,j>} \vec{S}_i \cdot \vec{S}_j \,, J > 0\,, \tag{2.2}$$

where $< i, j >$ runs over all nearest neighbors.
Let us now consider organizing a group of interacting spins on a lattice. Assuming the exchange coefficient between neighboring sites is $J > 0$, the nature of the ground state strongly depends on the type of lattice. If the lattice is bipartite, the ground state configuration yields neighboring spins to align in opposite direction and form a antiferromagnetically ordered Néel state. If the lattice is not bipartite, however, (meaning some triangular structures are present) the spins are unable to satisfy the minimization of energy on every bond by antiferromagnetic ordering, leading to a more exotic ground-state configuration.
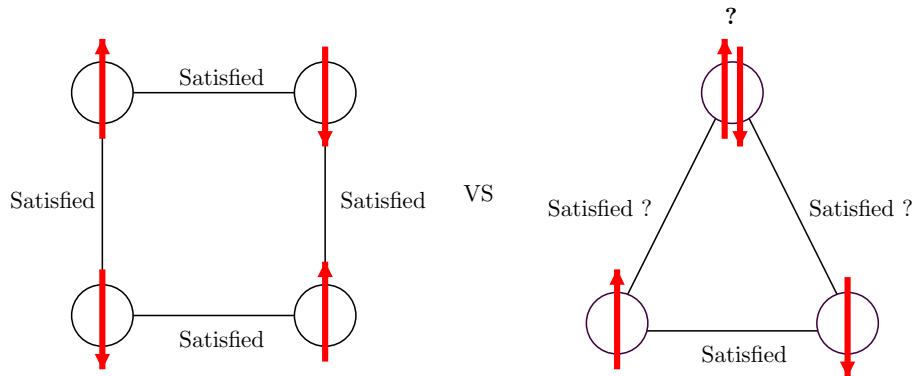
Figure 2.1: Illustration of frustration induced by the geometry of the cell: one of the three bonds of the triangular cell remains unsatisfied.

In the classical picture, comparing the unfrustrated square plaquette of the with the frustrated triangle in Fig. 2.1 another striking peculiarity emerges: while the degeneracy of the unfrustrated ground state is two-fold (configuration equivalent under global spin-flip), the degeneracy of ground state the frustrated variant in increased to six.

This can be understood from the following consideration: since the lowest possible energy is obtained with one of the three bonds not satisfied, evaluating the ground degeneracy is the combinatorial equivalent of calculating the number of permutations of three elements, two of them repeating (two satisfied bonds and one not satisfied).

$$P_3^{(2)} = \frac{3!}{2!} = 3 \,. \tag{2.3}$$

Counting the symmetry associated with spin means we need simply multiply the obtained numbers by two, yielding the desired result.

While this is of course merely an example, it turns out that, in a classical picture, frustration always induces degeneracy on the ground state manifold [19, pp. 8-10, 7]. It is precisely this increase in the ground state degeneracy that is responsible for the appearance of a lot of new and exotic physics in frustrated magnets. The quantum case is more complicated and variations in the degeneracy cannot be calculated by simple combinatorial operations. Some of the effects of quantum fluctuations in frustrated systems will be addressed later in this section. One paradigmatic example of the features of magnetic frustration is constituted by the Kagomé-Heisenberg antiferromagnet, illustrated in Fig. 2.2.
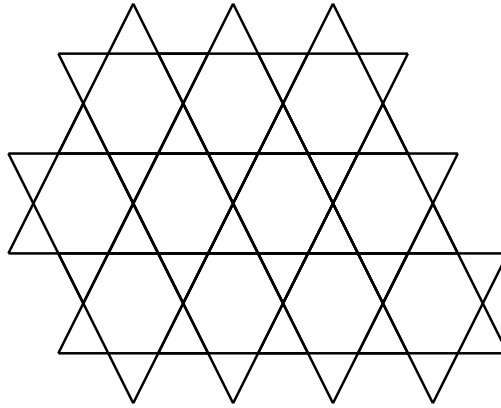
Figure 2.2: Illustration of the Kagomé lattice: each vertex of the lattice hosts a spin.

In the classical limit, energy minimization simply requires the total spin on each triangle to be zero [19, p. 208], rendering the ground state of the Kagomé antiferromagnet infinitely degenerate and the system extremely inclined to overall magnetic disorder. Considering the quantum nature of spins (specifically, $S = 1/2$), the situation is even more complex and no consensus regarding the actual nature of the ground-state has been reached yet. While there seems to be agreement on the disordered nature of the ground state, the discussion on the exact configuration is still open [20]: there are two potential ground state candidates, namely a gapless algebraic spin liquid phase [13], and a resonating valence bond $\mathbb{Z}_2$ spin liquid [37]. The name ,,spin liquid state" refers to the absence of symmetry breaking or magnetic ordering in the ground state of the Kagomé antiferromagnet and constitutes a completely new phase of matter.

Applying magnetic fields to a frustrated system and inspecting the magnetization curve can also reveal some intriguing features. The magnetization process of a Néel antiferromagnet is a very well understood phenomenon: considering the spins as classical vectors, the magnetization curve simply has a linear increase and a final saturation plateau.

Experimental results of magnetically frustrated spin systems, however, reveal great differences from the classical case characterized by the appearance of finite magnetization plateaus [19, pp. 241-260]. A magnetization plateau refers to phases, where the magnetization of the system remains unaffected from changes of the magnetic field strength at some finite value $M < M_{sat}$, as illustrated in Fig. 2.3.
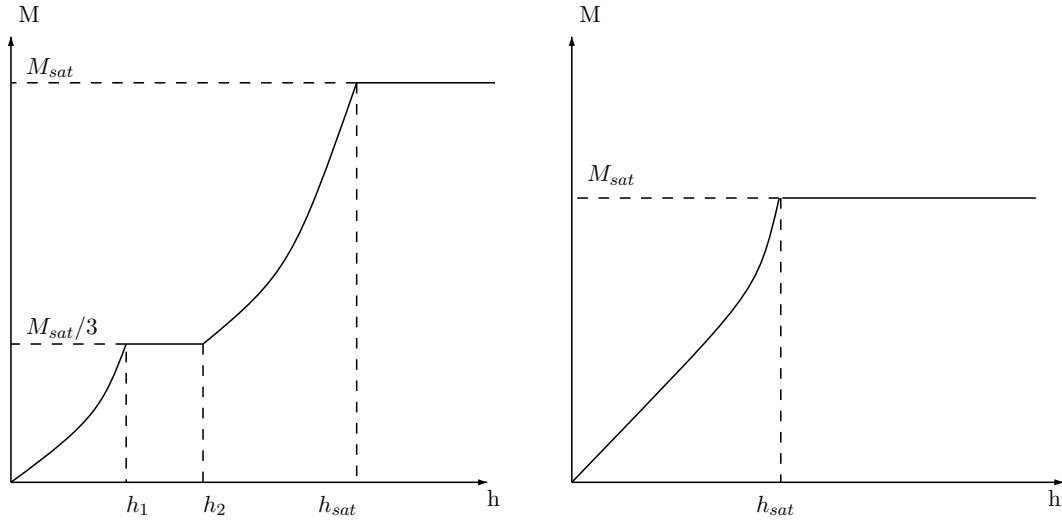
Figure 2.3: left panel: Magnetization curve of the triangular lattice. The system displays a magnetization plateau at $\frac{M_{sat}}{3}$; right panel: Magnetization curve of a typical unfrustrated antiferromagnet [19, p. 242].

We can sketch the occurrence of this phenomenon by briefly explaining the magnetization process on a triangular lattice under the influence of an external magnetic field. To this end, we consider a Heisenberg Hamiltonian with external field pointing in z-direction,

$$\hat{H} = \sum_{<i,j>} \vec{S}_i \cdot \vec{S}_j - h \sum_i \vec{S}_i^z \,. \tag{2.4}$$

In absence of the field, the ground features a planar order with all spins oriented 120° with respect to one another (see Fig. 2.4):
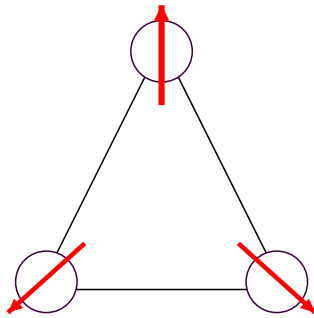

Figure 2.4: Classical ground state configuration of the spins at $h = 0$.

Increasing the magnetic field, many different ground-state configurations will satisfy energy minimization [1, 4]. In a purely classical picture the system continuously varies the orientation of the spins to reach saturation. The presence of quantum fluctuations in real atomic models, however, manages to alter the magnetization process by selecting coplanar states among the many possible ground state configurations of the classical case. The argument rests on a quasi-classical $1/S$ expansion [5]: the basic idea is to consider quantum fluctuations as perturbations of the classical configuration and then proceed by adding higher orders of the expansion,

$$E_0 = E_{class.} + E_{quant.} + \mathcal{O} \,. \tag{2.5}$$

If the influence of zero-point energy (energy associated with quantum uncertainty) becomes significant, quantum fluctuations end up stabilizing states that are classically to be excluded. In the case of the triangular lattice, the state that is favored by quantum fluctuations features 2 spins pointing parallel to the the field and 1 pointing in antiparallel direction [19, pp. 245-246, 4], as illustrated in Fig. 2.5
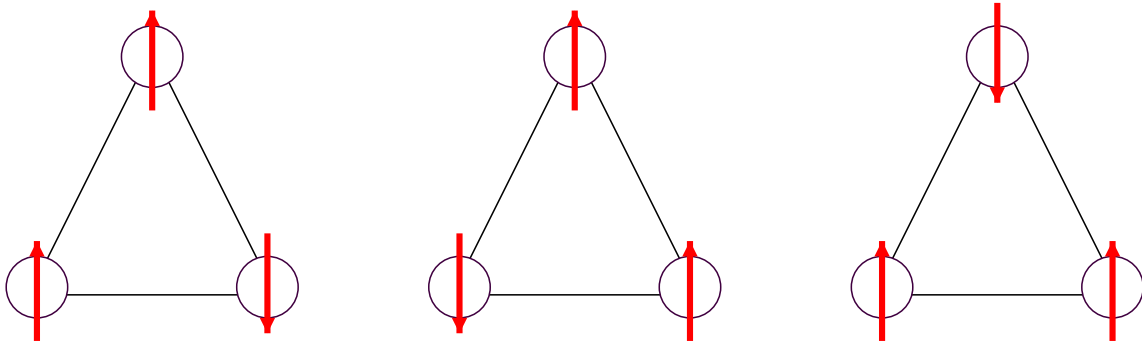

Figure 2.5: Spin configuration selected by quantum fluctuations.

This configuration represents the ground state order for an extended interval of the magnetic field (see Fig. 2.3) $h_1 \leq h \leq h_2$. Once the magnetic field is increased to values $h > h_2$, the plateau structure is broken off by the dominating Zeeman term in Eq. (2.4) and the spins get polarized towards saturation. Different lattices, however, reveal an even richer behavior with several magnetization plateaus [19, p. 255], all appearing at fractional or integer values of the saturation magnetization [19, p. 244].

2.2   The frustrated spin-$\frac{1}{2}$ ladder

Magnetic frustration is not only a theoretical phenomenon, but is actually present in a lot of compounds. Although we are able to directly probe these materials through magnetic neutron scattering [19, pp. 45-51, 26, pp. 10-21] or other techniques, fully understanding some of the exotic physical phenomena taking place requires us to break them down into minimal models because of the to high level of complexity of the real lattices. In other words, experimental results allow us to observe the effects, but to identify the causes from a theoretical standpoint, we need actual numerically solvable models that display similar proportions.

Here we are focusing on the frustrated spin 1/2 ladder, which is believed to capture some of the characteristics of the real compound $SrCu_2(Bo_3)_2$. The magnetic layer of this compound is displayed in Fig. 2.6
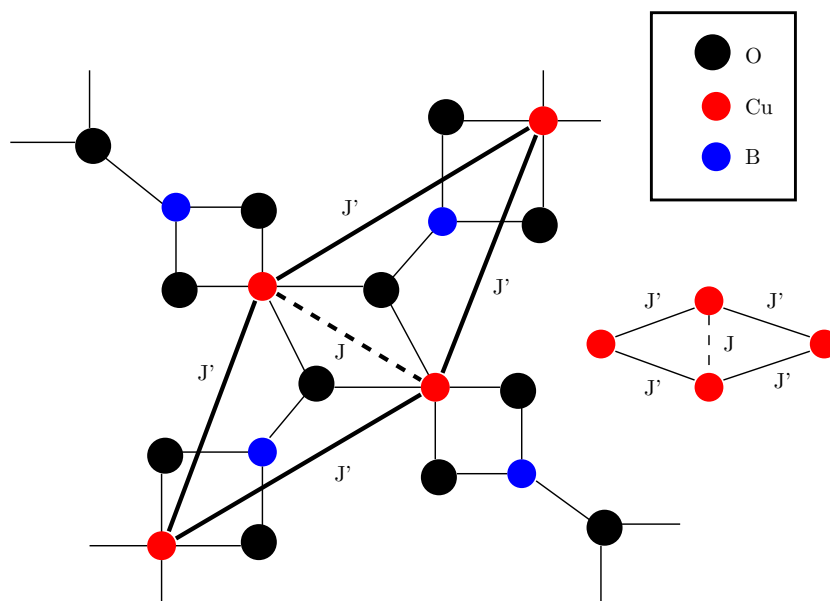

Figure 2.6: Magnetic layer of the $SrCu_2(Bo_3)_2$ compound. The atoms that actually have spin are the Cu^{2+}-ions (spin 1/2). The spins interact with one another through the other atoms. The system can be reduced to a spin lattice with nn (J) and nnn (J') interactions.

Its lattice structure is topologically equivalent to the so called ,,Shastry-Sutherland"
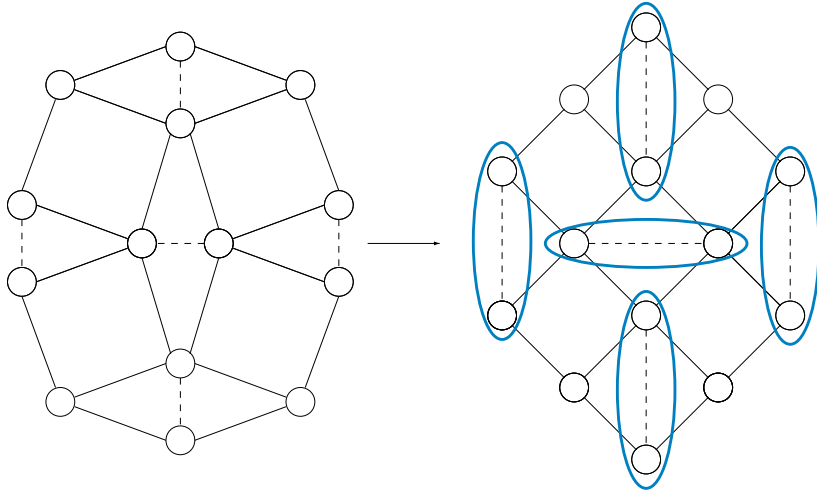lattice [19, pp. 520-522], illustrated in Fig. 2.7.

Figure 2.7: Left panel: effective spin lattice for the $SrCu_2(Bo_3)_2$ crystal. Right panel: through
a homotopy transformation, we can link the lattice to the Shastry-Sutherland geometry. The
blue ovals represent spin singlets. This configuration is known to be a ground state of this lattice
for $J'/J < 0.68$ [23].

Magnetic neutron scattering experiments reveal the gapped nature of the spectrum of this
geometry [17]. The ground state is known to be a spin-dimer configuration for $J'/J < 0.68$
(right panel of Fig. 2.7) [23]. The first excitation corresponds to the generation of a spin
triplet on one of the dimers and, as soon as temperature comes into play, this spectral feature
starts to lose considerable spectral weight. The reasons for the spectral weight decrease of
the first excited state remained unclear until recently, since the treatment of the excitation
spectrum of the full 2D model is numerically not feasable. Ref.[15] recently shed some light
into this issue by considering spin-1/2 frustrated ladder (Fig. 2.2), which, with the correct
combination of coupling parameters, is able to display an identical ground state configuration
and low energy regime.
The Hamiltonian of the frustrated spin-1/2 ladder has the following structure:

$$\hat{H} = \sum_i J_\perp \vec{S}_i^1 \vec{S}_i^2 + \sum_{i,m=1} (J_\parallel \vec{S}_i^m \vec{S}_{i+1}^m + J_\times \vec{S}_i^m \vec{S}_{i+1}^{\bar{m}}), \tag{2.6}$$

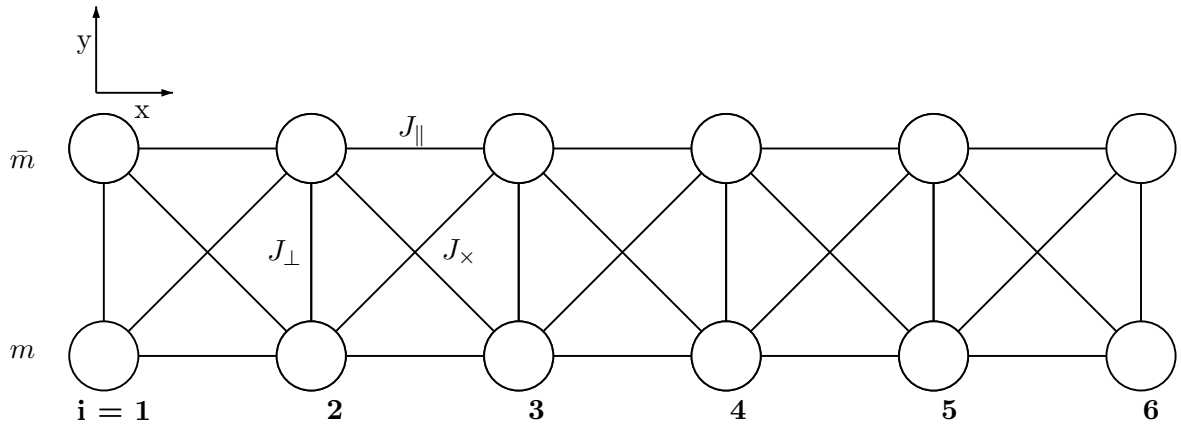$$J_\perp, J_\parallel, J_\times > 0. \tag{2.7}$$

Figure 2.8: Frustrated spin-1/2 ladder.

As all couplings are antiferromagnetic, each of the triangular plaquettes displays frustration. The fully frustrated case appears if we set $J_{\parallel} = J_{\times}$. In this configuration, the Hamiltonian can be rewritten [14] as

$$\hat{H}_F = J_{\perp} \left(\underbrace{\frac{J_{\parallel}}{J_{\perp}} \sum_{i=1}^{L} \vec{T}_i \cdot \vec{T}_{i+1}}_{\text{①}} + \underbrace{\sum_{i=1}^{L} \left(\frac{1}{2} \vec{T}_i^2 - S(S+1) \right)}_{\text{②}} \right),$$ (2.8)

where we introduced the new total spin rung operators $\vec{T}_i = \vec{S}_i^1 + \vec{S}_i^2$ and the spin quantum number per site $S = 1/2$. The model has already been studied under many aspects [15, 16]. One of the most striking peculiarities is the presence of two distinct phases of the ground state separated by a first order quantum phase transition (QPT) , i.e a phase transition that takes place at T = 0, driven solely by the relation $J_{\perp}/J_{\parallel}$. The two phases can be characterized by the distinct spin orientation on each rung.

Rung singlet phase: Each rung hosts a spin singlet meaning $\vec{T}_i^2 = 0 \ \forall i$, as illustrated in Fig. 2.9. This state has very similar properties to the ground-state of the Shastry-Sutherland lattice.
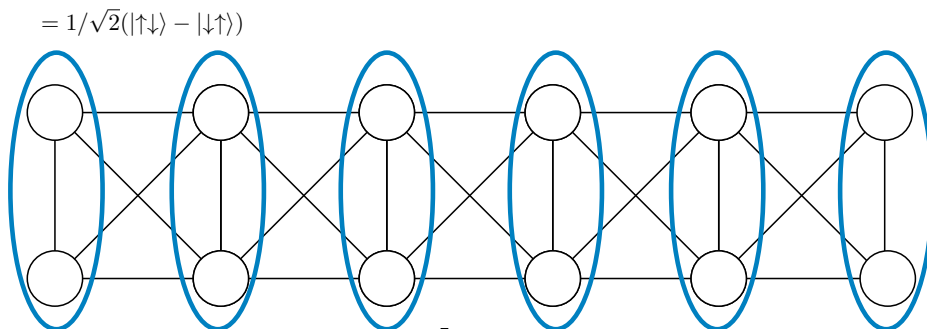

Figure 2.9: Singlet-phase ground states: each blue oval represents a rung singlet

Dimer or spin-triplet phase: The spins of each rung align yielding triplets: $\vec{T}_i^2 = 1 \ \forall i$, as illustrated in Fig. 2.10.
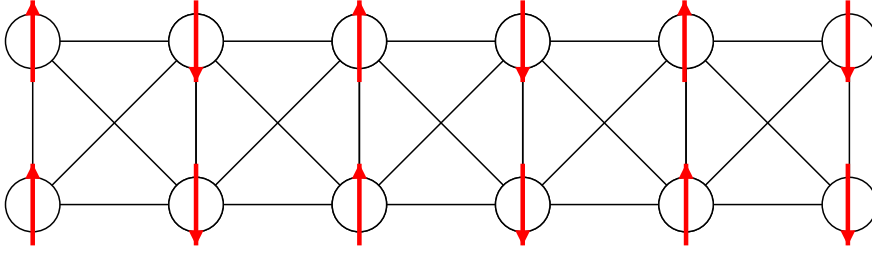
Figure 2.10: One of the possible triplet-phase ground states

Studying the Hamiltonian in Eq. (2.8) we can understand the origin of the two distinct phases. In the parameter regime $J_\perp \gg J_\parallel$, the term ② of Eq. (2.8) ends up dominating the Hamiltonian. In that case the minimum energy configuration would be $\vec{T}_i^2 = 0 \ \forall i$, leading to the singlet phase of Fig. 2.9. On the other hand, for $J_\perp \ll J_\parallel$ the term ① of Eq. (2.8) makes the biggest contribution the energy. In this case the energetically most favorable configuration yields an anti-aligned order on every $J_\parallel$ bond, resulting in the triplet phase (Fig. 2.10). To characterize these two different phases, we use the staggered magnetization (a magnetization per site that points along a certain quantization axis), which in the case of the spin ladder has the following form:

$$\hat{M}_{stag} = \frac{1}{N} \sum_l (-1)^l \vec{S}_l^z \, . \tag{2.9}$$

The index l represents the rung number and $\hat{S}_l^z$ the sum of the z-component of the spins on that particular rung. A singlet ground state $|\Psi\rangle_S$ will display $\langle\Psi|_S \hat{M}_{stag} |\Psi\rangle_S = 0$, whereas the triplet phase will be characterized by a non zero value of $\langle\hat{M}_{stag}\rangle$.

The parameters that tune the QPT are the coupling constants $J_\parallel$ and $J_\perp$ of the model [16]. The value for the critical coupling constant in the fully frustrated regime ($J_\parallel = J_\times$) can be derived theoretically [35] and has value $J_\perp/J_\parallel \approx 1.401484$ (in the thermodynamic limit).

A recent study based on exact diagonalization has been able to inspect the spectra of this particular system at $T = 0$ as well as at finite T up to lengths of 16 rungs [15]. Characterizing the influences of finite temperature on the excitation spectra for systems, which go beyond these system sizes, have however, not been successful due to the excessive numerical costs. Reduced ladder lengths may produce thermodynamic limit relevant data when the system is far away from the phase transitions because interaction lengths in these regimes are short. As we approach criticality though, a significant increase of the correlation length renders conclusions drawn on smaller systems not applicable to the thermodynamic limit, and thus, to realistic systems (see Chapter 4).

Recent developments in the field of matrix product states have provided us with a new toolbox enabling us to study energetic spectra of the spin ladder in the vicinity of the phase transition both at $T = 0$ and at finite temperature, where larger system sizes are necessary to faithfully approximate the thermodynamic limit.

3. Numerical methods

After having established the physical background of the underlying system, we need to discuss the numerical framework used to produce quantitative results. Here we discuss how to derive the excitation spectrum of the corresponding Hamiltonian by computing dynamical spin-spin correlators in the framework of matrix product states

3.1   Measuring method

Experiments can typically access the excitation spectrum of a compound by means of inelastic neutron scattering. In this section we derive the excitation spectrum of the spin ladder in terms of dynamical spin-spin correlators, which are experimentally accessible.
The assumption about our system is that the spins are fixed, allowing only for spin-spin interaction between the neutron and the sample. The measured observable, as in all scattering experiments, is the doubly differential cross section, which in the case of magnetic neutron scattering has the following from [19, pp. 50-53]

$$\frac{d^2\sigma}{dEd\Omega} = r_0^2 \frac{k_f}{k_i} f(\vec{Q})^2 \sum_{\alpha,\beta} (\delta_{\alpha\beta} - \hat{k}_\alpha \hat{k}_\beta) S^{\alpha\beta}(\vec{Q}, \omega). \tag{3.1}$$

This expression is a function that determines how many neutrons are being scattered in a differential solid angle $d\Omega$ and how many of these have an energy contained in the energy shell dE. A peak in the differential cross section implies that a large number of neutrons are scattered in this particular energy shell, meaning that the energy transfer between probing neutron and sample drives the system into an excited state. A peak in the differential cross section corresponds to an excitation level of the sample spectrum. In order to understand where the peaks may arise, we need to inspect the tensor $S^{\alpha\beta}(\vec{Q}, \omega)$, which is called the dynamic structure factor [26, pp. 135-138],

$$S^{\alpha\beta}(\vec{k},\omega) = \frac{1}{2\pi} \sum_{\vec{R}} \int_{-\infty}^{\infty} e^{i(\vec{k}\cdot\vec{R}+\omega t)} \underbrace{\langle S_0^\alpha(t=0) S_{\vec{R}}^\beta(t)\rangle}_{S_{\equiv\vec{R}}^{\alpha\beta}(t)} dt, \tag{3.2}$$

where $\vec{k}$ is a momentum, ω an energy and $\vec{R}$ the real space lattice vector.
Eq. (3.16) is the space time Fourier transform of the time dependent spin-spin correlation function of the sample. Time is being treated as a continuous variable, while space is a discrete variable (the spins are located on a lattice with spacing $a = 1$). In the case of the spin ladder in Eq. (2.6) the structure factor can be simplified [3]:

11

$$S_{k_y=0}^{\alpha\beta}(k,\omega) = \sum_l \int_{-\infty}^{\infty} e^{i(\omega t - kl)} \langle S_{0,k_0}^{\alpha}(t=0) S_{l,k_0}^{\beta}(t) \rangle \, dt \,, \tag{3.3}$$

$$S_{k_y=\pi}^{\alpha\beta}(k,\omega) = \sum_l \int_{-\infty}^{\infty} e^{i(\omega t - kl)} \langle S_{0,k_\pi}^{\alpha}(t=0) S_{l,k_\pi}^{\beta}(t) \rangle \, dt \,. \tag{3.4}$$

We discretize space in one dimension ($\vec{R} \to l$ = rung number) and restrict the possible values of the momentum in $y-$direction to $q_y \in \{0, \pi\}$. The second simplification stems from the structure of the ladder:

$$\vec{k} = \begin{pmatrix} k_x \\ k_y \end{pmatrix} = 2\pi \begin{pmatrix} n_x/L_x \\ n_y/L_y \end{pmatrix}, \tag{3.5}$$

$$L_x = L/2, \, L_y = 2 \,, \tag{3.6}$$

$$n_x \in \{0, \cdots, L_x\}, \, n_y \in \{0, 1\} \,. \tag{3.7}$$

In the scope of this thesis the two distinct tensors (3.3) and (3.4) will be calculated and displayed separately. The reason for this distinction is that the combination of selection rules for neutron scattering ($\Delta S = 0, \pm1$) and conservation laws of spin on each rung ensure different excitation are visible in different channels [15]. For instance, direct processes in the singlet ground state phase, i.e, the ones where the total number of triplets changes from $n \to n, n+1$ as a consequence of neutron-spin interaction are only visible in the antisymmetric channel.
In numerical practice the time variable will be discrete and limited, thus

$$t \in \mathbb{R} \to t_n = n\Delta t, n \in \{0, 1, 2, \cdots, N\} \,, \tag{3.8}$$

$$S_{k_y}^{\alpha\beta}(k,\omega) \approx \sum_{n=-N_t+1}^{N_t} \sum_{l=-L/2+1}^{L/2} e^{i(\omega t_n - kl)} S_{l,k_y}^{\alpha\beta} \Delta t \,, \tag{3.9}$$

$$\langle S_{0,k_\pi}^{\alpha}(t=0) S_{l,k_\pi}^{\beta}(t) \rangle = \langle \Psi | \, e^{it_n \hat{H}} S_{l+L/2,m}^{\beta} e^{-it_n \hat{H}} S_{L/2,m}^{\alpha} \, |\Psi\rangle \,. \tag{3.10}$$

The l index identifies on which rung we are on, while the wave equation $|\Psi\rangle$ in Eq. (3.10) can represents the ground state or a thermal state of the Hamiltonian.
In order to mitigate the finite-time effects on the discrete Fourier transform, we apply a Gaussian filter [3] with a line broadening parameter $\eta = 2/t_N$:

$$g(t_n) = e^{-(t_n\eta)^2} \,, \tag{3.11}$$

$$S_{k_y}^{\alpha\beta}(k,\omega) \approx \sum_{n=-N_t+1}^{N_t} \sum_{l=-L/2+1}^{L/2} e^{i(\omega t_n - kl)} \underbrace{g(t_n) S_{l,k_y}^{\alpha\beta}}_{\to S_{l,k_y}^{\alpha\beta}} \Delta t \,. \tag{3.12}$$

In the next section, we will elaborate on the numerical framework employed in this thesis to numerically simulate Eq. (3.12).

3.2 Matrix product states

The framework of matrix product states (MPS) forms the building blocks of some of the most powerful numerical methods for 1D quantum systems that are also employed in this thesis. Based on MPS, we determine the ground state by means of the density matrix renormalization group (DMRG). The ground state of the spin ladder is taken as starting point to compute the dynamical spin structure factor at $T = 0$ using real-time evolution via time-dependent DMRG (tDMRG). To extract the dynamics of the model at finite temperatures, we use density-matrix purification to obtain the thermal density matrix, which is again time evolved using tDMRG. In this section, we give a brief introduction to these numerical techniques and sketch their main concepts. For a detailed description we refer to the reviews [25, 22].

3.2.1 Diagrammatic representations

In order to understand the above mentioned numerical techniques (DMRG and tDMRG), it is helpful to introduce the framework of matrix product states (MPS). Many steps of MPS methods can greatly be simplified by using a diagrammatic representation of the underlying mathematical equations, which we briefly introduce in the following.
MPS and other tensor networks parametrize the wavefunction of a quantum many-body system by a set of multidimensional tensors. A tensor is a multidimensional array of numbers, and can be pictorially represented as in Fig. 3.1.
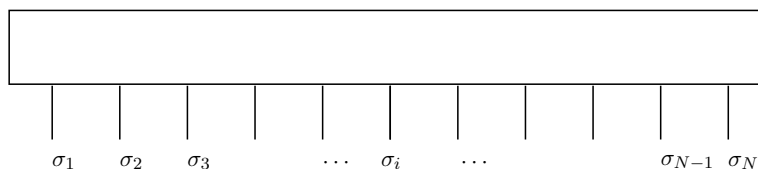

Figure 3.1: Diagrammatic representation of an N-dimensional tensor.

In this diagrammatic representation, the legs sticking out identify the indices σ_i of the tensor. In general, tensors can be obtained from contraction of other tensors. Tensor contraction are diagrammatically represented as follows (Fig. 3.2) throughout this project:
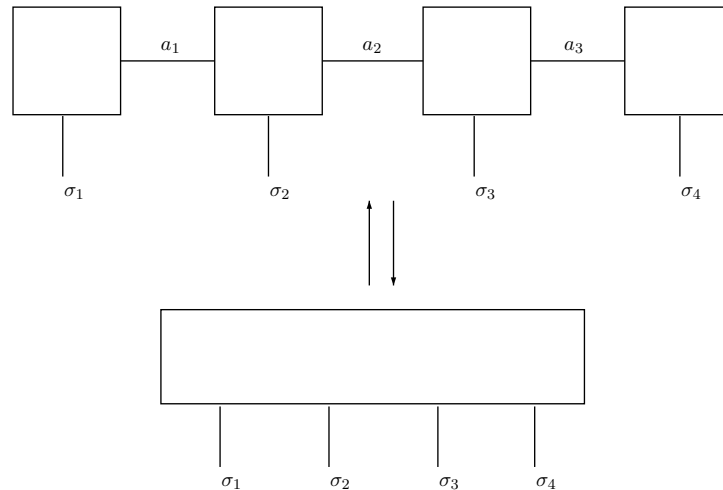
Figure 3.2: Complex tensor contraction.

A leg connecting two tensors implies that we are summing over this particular index. The legs that remain sticking out are the relevant ones: they define the dimension of the resulting tensor. By adopting this convention, we can reduce complex tensor contractions involving lengthy mathematical equations to simple diagrams. For instance, the diagram of Fig. 3.3
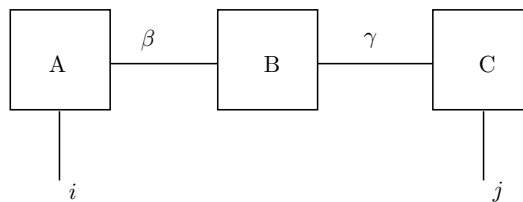

Figure 3.3: Diagrammatic representation of a combined matrix multiplication.

actually stands for the expression.

$$D_{ij} = \sum_{\beta\gamma\delta} a_{i\beta} b_{\beta\gamma} c_{\gamma j} \,, \tag{3.13}$$

see Appendix 6.1 for the procedure or refer to Ref. [25, pp. 19-24] for a complete overview of the methodology.

3.2.2   MPS generalities

We will now give a brief introduction to the matrix product state representation of quantum many-body states. Let us consider an arbitrary pure many-body quantum state of a system with L sites:

$$|\psi\rangle = \sum_{\sigma_1\cdots\sigma_L} \Psi_{\sigma_1\cdots\sigma_L} |\sigma_1\cdots\sigma_L\rangle \,, \ \sigma_i = 1,\cdots,d \ \forall\, i \,. \tag{3.14}$$

The state is defined by its wave equation coefficient tensor $\Psi_{\sigma_1 \cdots \sigma_L}$ in combination with the Fock state $|\sigma_1 \cdots \sigma_L\rangle$. The key idea of an MPS representation is to express $\Psi_{\sigma_1 \cdots \sigma_L}$ set of three-dimensional tensors M^{σ_i} leading to the following form.

$$|\psi\rangle = \sum_{\sigma_1 \cdots \sigma_L} M^{\sigma_1} M^{\sigma_2} \cdots M^{\sigma_L} |\sigma_1 \cdots \sigma_L\rangle . \tag{3.15}$$

The diagrammatic representation of Eq. (3.15) immediately yields Fig. 3.4.
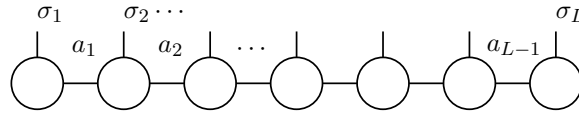
Figure 3.4: MPS form of a pure quantum state.

What are the main advantages of the MPS representation of the wave function? First of all, we are talking about physically relevant solid state models, which attempt to capture the behaviors on the atomic scale. The dimension of the Hilbert space grows exponentially with system size L and so does the number of wave-function coefficients. In the MPS representation one can avoid this exponential scaling by introducing an upper cutoff dimension D (the so-called bond dimension) limiting the sizes of the M tensors in Eq. (3.15). In this way, the numerical costs of the MPS only scale polynomially with system size, which is the key to the effectiveness of many MPS approaches.

One other great advantage of the MPS representation is the way it encodes information about quantum entanglement. In the normal algebraic representation, determining whether a wave function encodes entanglement typically cannot be naturally deduced. Our newly introduced formalism on the other hand, captures information about entanglement in a natural and convenient way.

To further elaborate on these statements, we again consider the MPS representation of the many-body state in Eq. (3.15). Cutting the system up in two parts and writing the wave function in terms of this bipartite system leads to:

$$|\psi\rangle = \sum_{ij} \Psi_{ij} |i\rangle_A \otimes |j\rangle_B , \tag{3.16}$$

or, in the Schmidt-basis (see Appendix 6.2)

$$|\psi\rangle = \sum_{a=1}^{r} s_a^2 |a\rangle_A \otimes |a\rangle_B , \tag{3.17}$$

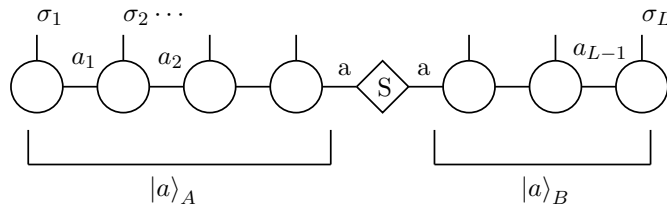which is diagrammatically represented is Fig. 3.5

Figure 3.5: Diagrammatic representation of the Schmidt-decomposition of a pure quantum state. This is also known as the bond-canonical form of an MPS [25, p. 23].

We compute the reduced density matrix for subsystem A:

$$\hat{\rho}_A = Tr_B(|\Psi\rangle \langle\Psi|) = \sum_{a=1}^{r} s_a^2 |a\rangle_A \langle a|_A. \tag{3.18}$$

This procedure can be repeated analogously for $\hat{\rho}_B$. If we assume a to have at most bond dimension D, the size of density matrix is upper bound by D.

$$\hat{\rho}_A = \sum_{a=1}^{D} s_a^2 |a\rangle_B \langle a|_B. \tag{3.19}$$

The amount of entanglement in the system can be expressed by computing the so-called von-Neumann entropy, which in this basis has the simple form,

$$S_{A|B} = -Tr_A[\hat{\rho}_A log_2(\hat{\rho}_A)] = -Tr_B[\hat{\rho}_B log_2(\hat{\rho}_B)] = -\sum_{a=1}^{D} s_a^2 log_2(s_a^2). \tag{3.20}$$

As a consequence of Eq. (3.19), entanglement entropy is also bound by the bond dimension D.

At this point the relationship between bond dimension and entanglement entropy emerges with clarity.

- $D = 1 \Rightarrow S_{A|B} = 0$: The quantum state is not entangled.

- $D > 1 \Rightarrow S_{A|B} > 0$: The quantum state is entangled.

We should remark that a bond dimension $D > 1$ is an indicator of entanglement but it does not give information about the degree of entanglement, namely, given two MPS in the Schmidt-basis with bond dimensions D_1 and D_2

$$D_1 > D_2 \nRightarrow S_{A|B,1} > S_{A|B,2}. \tag{3.21}$$

The degree of entanglement depends on the distribution of the eigenvalues of the density matrix s_a^2 in Eq. (3.20): the closer to an equipartition distribution, the higher the degree of entanglement $S_{A|B}$.

At this point we should make some remarks as to under which circumstances we are able to work with this formalism and retrieve useful data.

It can be shown [22] that, for an arbitrary quantum state, the dimension of the tensors composing the network will grow exponentially with the size of the system. Imposing an upper threshold D for the bond dimension is therefore strictly necessary in order to ease the exponential scaling and allow for a numerically feasible MPS representation [25, pp. 45-50, 21]. However, this raises some concern since in this procedure we have to truncate large parts of the Hilbert space that could potentially be important for an accurate representation of the wavefunction.

Fortunately it turns out that in many physically relevant Hamiltonians (i.e., ones with short-ranged interactions) the MPS can still capture the entanglement properties of low-energy and thermal states faithfully. It has been demonstrated, that different Hamiltonians possess different scaling properties of the entanglement entropy with respect to system size for different energy scales. These properties can be formalized in terms of so-called volume- and area laws [8]. Generic states of most Hamiltonians follow the volume law, i.e. given a bipartite

system $A|B$ with spatial dimension M, the entanglement entropy of these states $S_{A|B} \propto L^M$. For Hamiltonians with short-range interactions though, it can be shown [11] that the low-lying energy states of this particular class of systems obey an area law scaling of the entanglement entropy $S_{A|B} \propto L^{M-1}$. To analyze the worst case scenario, we maximize the expression for entanglement entropy in Eq. (3.20) by setting $s_a^2 = 1/D \; \forall \, a$

$$S_{A|B} = log_2(D) \Rightarrow D = 2^{S_{A|B}} \,. \tag{3.22}$$

If we are dealing with a $2D$ $(M = 2)$ system, L identifies the side length and the area law for the low-energy regime states that $S_{A|B}(L) \propto L$ which implies $D(L) \propto 2^L$. The bond dimension experiences exponential growth with L, meaning that MPS truncation will yield an uncontrollable error. If however, our system is $1D$ $(M = 1)$, $S_{A|B}(L) \propto 1$ which means $D(L) = const.$. This is an important result, as is states that one-dimensional systems allow us to truncate the bond dimension to a finite value without sacrificing excessive accuracy of the results.

The Hamiltonian describing the frustrated spin ladder does not fall exactly in this category since the interactions go beyond simple next neighbor exchange. As we will discover in the next sections however, we will be able to re conduct it to a system perfectly suitable with the MPS formalism.

3.2.3 Evaluation of observables

One of the reasons MPS are very popular in numerical treatments, is because of one can easily and accurately implement overlaps and expectation values. The overlaps we are dealing with in the scope of this project involve mainly local operators such as:

$$\langle\Psi_0| \hat{S}_{l+L/2,m}^{\beta}(t_n)\hat{S}_{L/2,m}^{\alpha} |\Psi_0\rangle \;\; \text{(zero temperature)}\,, \tag{3.23}$$

$$\langle\Psi_T| \hat{S}_{l+L/2,m}^{\beta}(t_n)\hat{S}_{L/2,m}^{\alpha} |\Psi_T\rangle \;\; \text{(finite temperature)}\,. \tag{3.24}$$

Since these involve time evolution in the form of $e^{i\hat{H}t}$, evaluating them requires further background knowledge which will be provided in the tDMRG section (Section 3.5). Here we will concentrate on the evaluation of time independent observables, in particular correlators. A local operator is one only acting on one of the sub-spaces:

$$\hat{O}^{[i]} = \sum_{\sigma_i,\sigma_i'} O_{\sigma_i\sigma_i'} |\sigma_i'\rangle \langle\sigma_i| \,. \tag{3.25}$$
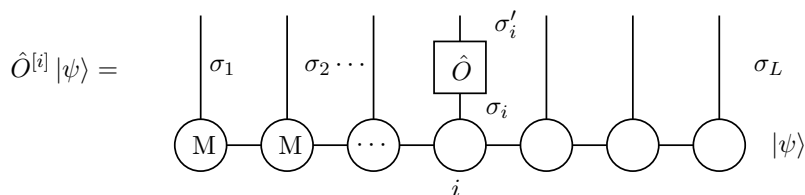

Figure 3.6: Local operator acting on an MPS.

A generic correlator calculation in MPS formalism has the following structure:

$$\langle\phi|\,\hat{O}^{[i]}\hat{P}^{[j]}\,|\psi\rangle = \sum_{\substack{\sigma_1\cdots\sigma_i\cdots\sigma_j\cdots\sigma_L \\ \sigma_i'\sigma_j'}} \tilde{M}^{\sigma_1\dagger}\cdots\tilde{M}^{\sigma_i'\dagger}\cdots\tilde{M}^{\sigma_j'\dagger}\cdots\tilde{M}^{\sigma_L\dagger}O_{\sigma_i\sigma_i'}P_{\sigma_j\sigma_j'}M^{\sigma_1}\cdots M^{\sigma_L}\,.$$
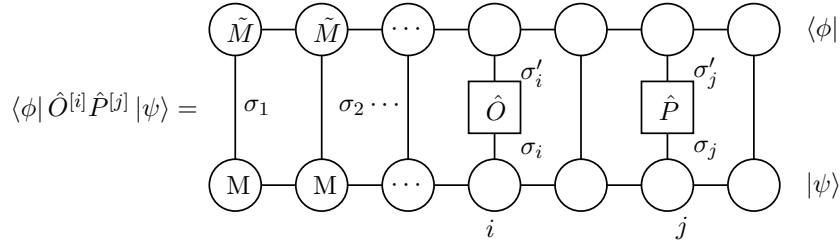
(3.26)

Figure 3.7: Matrix element of the correlator in diagrammatic representation.

Evaluating this number amounts to a complex tensor contraction. It should be noted that simply performing this contraction without taking in account the order might result in an exponential increase of the numerical costs with the system size [25, pp. 34-36]. Organizing the contraction in the following scheme, however, reduces the cost to a linear dependence on system size:
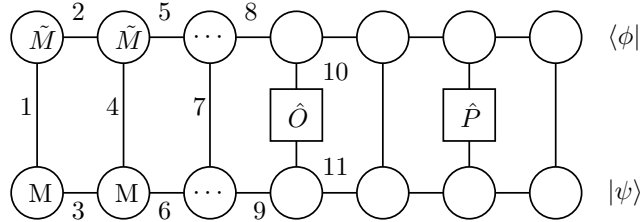
Figure 3.8: Convenient contraction order.

For the details about the correct contraction order we refer to the review [25, pp. 34-36]

3.3   Mapping the ladder onto a chain

Although MPS are ideally suited to represent one-dimensional systems, they work fairly well when applied to two-dimensional systems with finite width L_y (albeit the numerical costs scale exponentially with the width). In case of the spin ladder, the width of the system is fairly small, $L_y = 2$, and an MPS treatment still works well.
To make the system amenable for MPS, we have to map the ladder onto a chain with longer-ranged interactions.
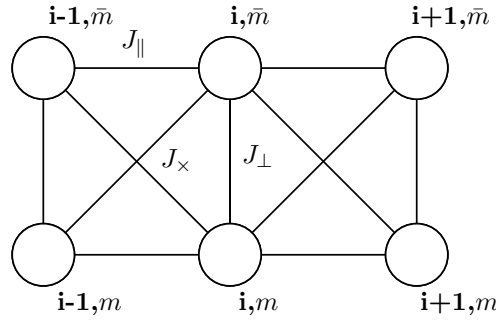
Figure 3.9: A segment of the spin-1/2 ladder.

Consider a segment of the spin ladder shown in Fig. 3.9, where we observe that sites at rung i interacts with 5 other sites. If we map the spin ladder onto a spin chain, some of the interaction terms, that in the original setup coupled nearest-neighbor sites, now become longer ranged, as illustrated in Fig. 3.10. However, since the interaction strengths (J) do not depend on the geometry of the lattice, the two structures are inherently equivalent.
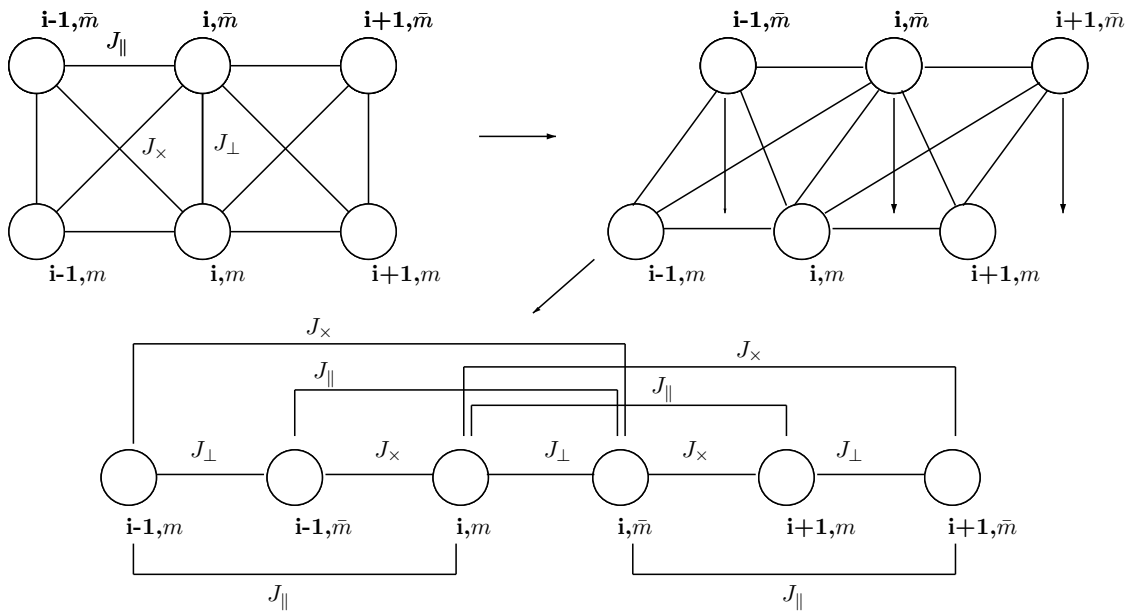

Figure 3.10: Illustration of the chain mapping for the spin ladder model.

The cost of the mapping operation lies in the longer-ranged interactions that occur in the chain. These will have consequences for the entanglement of the wave function and for the technical setup of the DMRG and tDMRG calculations.

3.4 DMRG in MPS formalism

In order to compute the dynamic structure factor at zero temperature, we need to determine the ground state of the Hamiltonian. While exact diagonalization approaches are indeed possible, the exponential growth of the many body Hilbert space dimension limits their use to small systems. Finite size density matrix renormalization group (DMRG) is a variational

method designed to obtain the ground state of high-dimensional Hamiltonians such as the ones appearing in many body quantum physics.

DMRG was introduced by Steve White prior [31] to the development of MPS and TN methods. As it turn out, the success of DMRG is routed in the implicit MPS structure of the algorithm and the explicit formulation of DMRG in the MPS framework lead to the development of many powerful extensions and improvements of the algorithm. From the historic perspective, one normally starts by describing the variant of DMRG that treats infinitely long systems (infinite-size DMRG) and then focuses of the finite-size variant of the algorithm. Since we only treat chains of finite length in the scope of this thesis, we focus on the finite-size algorithm only. We refer to Schollwoeck's review for a more complete discussion of the topic [25].
Consider a Hamiltonian $\hat{H}$. To determine its ground state $|\psi_0\rangle \in \mathcal{H}$ we follow a variational procedure.

$$
\begin{aligned}
\hat{H} |\psi_0\rangle &= E_0 |\psi_0\rangle \,, & (3.27) \\
\Rightarrow \langle\psi| \hat{H} |\psi\rangle &\geq E_0 \langle\psi|\psi\rangle \,, & (3.28) \\
\Rightarrow |\psi_0\rangle &= \arg \min_{\langle\psi|\in\mathcal{H}} \left(\langle\psi| \hat{H} |\psi\rangle - \lambda \langle\psi|\psi\rangle \right) . & (3.29)
\end{aligned}
$$

The Lagrange multiplier λ ensures ground state normalization. Assuming we are able to produce the matrix product operator (MPO) representation of the Hamiltonian [25, 22], Eq. (3.29) can be depicted by TN diagrams in Fig. 3.11
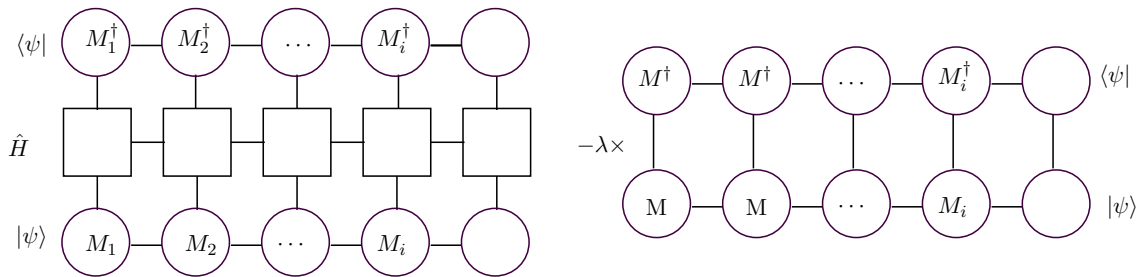

Figure 3.11: Diagrammatic representation of the minimization problem in Eq. (3.29).

The variables of this problem are the tensors M_i composing the wave function: they constitute the parameters that, upon variation, yield lower and lower energies. Naively we could try varying all the tensors simultaneously in order to obtain the correct ground state but this approach implies solving a highly non linear optimization problem, which cannot be numerically solved for large system sizes. Here the key idea of DMRG comes into play: instead of treating the tensors globally, we start from a random set of tensors and minimize the system one tensor at the time, updating the MPS wave function at each step.
The iterational ground state search algorithm has the following structure:

$$\text{sweep 1: left} \quad \rightarrow \quad \text{rigth} \tag{3.30}$$

$$|\tilde{\psi_0}\rangle^{[1]} \quad = \quad \arg \min_{M_1}(\langle\psi|\,\hat{H}\,|\psi\rangle - \lambda\,\langle\psi|\psi\rangle)\,, \tag{3.31}$$

$$|\tilde{\psi_0}\rangle^{[2]} \quad = \quad \arg \min_{M_2}\left(\langle\tilde{\psi_0}|^{[1]}\hat{H}|\tilde{\psi_0}\rangle^{[1]} - \lambda\,\langle\tilde{\psi_0}^{[1]}|\tilde{\psi_0}^{[1]}\rangle\right), \tag{3.32}$$

$$\vdots \tag{3.33}$$

$$|\tilde{\psi_0}\rangle^{[L]} \quad = \quad \arg \min_{M_L}\left(\langle\tilde{\psi_0}|^{[L-1]}\hat{H}|\tilde{\psi_0}\rangle^{[L-1]} - \lambda\,\langle\tilde{\psi_0}^{[L-1]}|\tilde{\psi_0}^{[L-1]}\rangle\right). \tag{3.34}$$

Once we have reached the end of the system, we revert the algorithm and proceed from right to left in what is known as "sweeping" through the system.

$$\text{sweep 2: right} \quad \rightarrow \quad \text{left} \tag{3.35}$$

$$|\tilde{\tilde{\psi}}_0\rangle^{[L+1]} \quad = \quad \arg \min_{M_{L-1}}\left(\langle\tilde{\psi_0}|^{[L]}\hat{H}|\tilde{\psi_0}\rangle^{[L]} - \lambda\,\langle\tilde{\psi_0}^{[L]}|\tilde{\psi_0}^{[L]}\rangle\right), \tag{3.36}$$

$$|\tilde{\tilde{\psi}}_0\rangle^{[L+2]} \quad = \quad \arg \min_{M_{L-2}}\left(\langle\tilde{\tilde{\psi}}_0|^{[L+1]}\hat{H}\,|\tilde{\tilde{\psi}}_0\rangle^{[L+1]} - \lambda\,\langle\tilde{\tilde{\psi}}_0^{[L+1]}|\tilde{\tilde{\psi}}_0^{[L+1]}\rangle\right), \tag{3.37}$$

$$\vdots \tag{3.38}$$

$$|\tilde{\tilde{\psi}}_0\rangle^{[2L]} \quad = \quad \arg \min_{M_2}\left(\langle\tilde{\tilde{\psi}}_0|^{[2L-1]}\hat{H}\,|\tilde{\tilde{\psi}}_0\rangle^{[2L-1]} - \lambda\,\langle\tilde{\tilde{\psi}}_0^{[2L-1]}|\tilde{\tilde{\psi}}_0^{[2L-1]}\rangle\right). \tag{3.39}$$

The importance of this scheme, is that it allows us to reduce a non-linear optimization problem in a series of linear optimization problems. The minimization equation can in fact be rewritten in terms of matrix products:

$$\min_{M_i}(\langle\psi|\,\hat{H}\,|\psi\rangle - \lambda\,\langle\psi|\psi\rangle) = \min_{M_i}(M_i^\dagger\hat{H}_{eff}M_i - \lambda M_i^\dagger N M_i)\,, \tag{3.40}$$

assuming canonical form of the MPS [25], we can reformulate the minimization problem in a generalized eigenvalue problem:
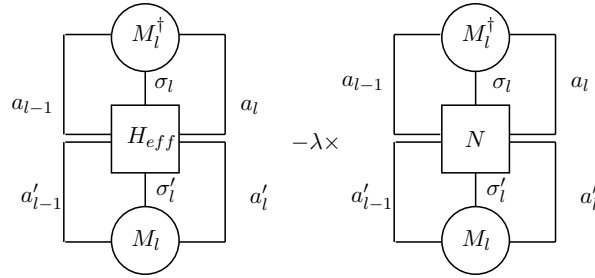

Figure 3.12: Minimization at site l: all tensors $\neq M_l, M_l^\dagger$ are absorbed either in an effective Hamiltonian $\hat{H}_{eff}$ or in the normalization matrix N

At this point we search for the minimum by forming the partial derivative with respects to $M_l^\dagger$ and obtain a generalized eigenvalue problem:

$$\frac{\partial}{\partial M_i^\dagger}(M_i^\dagger\hat{H}_{eff}M_i - \lambda M_i^\dagger N M_i) \quad = \quad 0\,, \tag{3.41}$$

$$\Rightarrow \hat{H}_{eff}M_i - \lambda N M_i \quad = \quad 0\,. \tag{3.42}$$

Since we are interested in the matrix M_l that minimizes λ, we only need to compute the smallest eigenvalue. This kind of problem can be tackled with the Lanczos method [18] and costs much less in numerical terms than a complete diagonalization. Once we have minimized M_l, we will update the MPS and proceed to the next iteration, where our goal will be to minimize M_{l+1}. The minimization of each individual matrix ensures we obtain lower and lower energies at every iteration, however the number of sweeps one needs to perform before the energy converges is heavily dependent the specific system.

As much as this new approach for the ground state search might seem attractive, we should keep in mind that, much like many other numerical methods, it has its strengths and weaknesses [25]. Finally, we need to briefly discuss how some spectral features of the Hamiltonian may negatively influence the validity of the produced results. Consider a parameter regime of some Hamiltonian that yields a very small excitation gap with an almost continuous distribution of excited states above the ground state. If we apply finite-size DMRG in this situation, we may notice that we need a lot of sweeps before witnessing convergence. This can be attributed to the large number of states with very similar energies in the vicinity of the ground state. This particular aspect will be further discussed in chapter 4.

3.5   tDMRG

With DMRG we can obtain the ground state of the spin ladder across the entire phase diagram. The latter is the starting point for the calculation of the dynamic spin structure factor at zero temperature, which now has to be evolved in real time before applying a Fourier transform. Evaluating the time evolution of a pure quantum state constitutes yet another strength of the MPS formalism [33, 6, 29].

The time-dependent Schrödinger equation allows us to write the time evolution operator as follows:

$$|\psi(t)\rangle = e^{-i\hat{H}t} |\psi(0)\rangle \ . \tag{3.43}$$

Several techniques apart from the here discussed tDMRG (see tMPS and TEBD in Ref. [25, pp. 75-84] for a review) have been developed to deal with this problem, each with its strengths and weaknesses depending on the kind of Hamiltonian determining the dynamics.

Mapping the spin ladder onto a chain has increased the of interaction range of some bonds (see Fig. 3.10) which increases the technical complexity of MPS-based time evolution. However, the time evolution in this system can still be performed in terms of a Suzuki-Trotter composition, which has proven to be highly successful for systems with nearest-neighbor interaction only. In this section, we elaborate on standard MPS time evolution before discussing how to incorporate longer-ranged interaction terms by means of swap gates.

3.5.1   Nearest-neighbor interaction

If the Hamiltonian that determines the dynamics of the system only depends on nearest-neighbor interaction, it can be factorized as follows:

$$\hat{H} = \sum_{i}^{L-1} \hat{h}_i \ , \tag{3.44}$$

where $\hat{h}_i$ encodes the interaction between sites i and $i+1$. Splitting the total time evolution in N smaller time steps $\tau = t/N$ enables us to express the time evolution operator by a set

of local gates using a first-order Suzuki-Trotter decomposition [12]:

$$
e^{-i\hat{H}t} = \left(\prod_{i=1}^{L-1} e^{-i\hat{h}_i\tau} + \mathcal{O}(\tau^2) \right)^N .
\tag{3.45}
$$

The non-commutativity of the local operators is accounted for by inserting the so-called ,,Trotter-error" term of quadratic order in the time step. Eq. (3.45) is known as a first order Suzuki-Trotter decomposition of the time evolution operator.

The magnitude of the Trotter-error can be further reduced by selecting higher order Suzuki-Trotter approximations [12]. In this thesis, for instance, we used a second order Suzuki-Trotter decomposition, which has the form

$$
e^{-i\hat{H}t} = \left(\prod_{i=1}^{L-1} e^{-i\hat{h}_i\tau/2} \prod_{i=L-1}^{1} e^{-i\hat{h}_i\tau/2} + \mathcal{O}(\tau^3) \right)^N .
\tag{3.46}
$$

In this approximation, the time evolution process of the MPS can be visualized by the diagram in Fig. 3.13
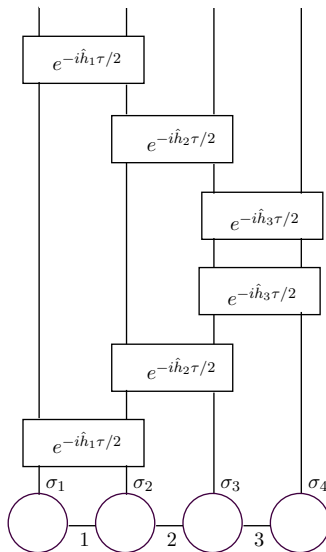
Figure 3.13: One time step τ performed with a second order Suzuki-Trotter decomposition on a MPS of with $L = 4$.

It should be noted that the time evolution operator increases the bond dimension of the MPS at each application $e^{-i\hat{h}_i\tau/2}$ [25]. In order to prevent the computational costs from growing exponentially, we have to apply a truncation procedure after each bond evolution, which yields a truncation error. The Trotter error and the truncation error are the two main limiting factors of the time evolution of an MPS. However, while the trotter error can be controlled by reducing the time step τ or by using a higher order Trotter approximation, the truncation error grows exponentially in time [25], making it the main limiting factor for the reliability of the time evolution calculations.

3.5.2   Beyond next-neighbor interactions

The previously introduced formalism derives all its conclusions on the assumption that the Hamiltonian can be written as a sum of next-neighbor terms.
However, if a Hamiltonian accounting for interactions that go beyond next-neighbor only includes two-site interaction, one can still rely on a Trotter decomposition to perform the time evolution by introducing so-called swap gates [27, pp. 6-8]. A swap gate simply switches the physical indexes of two adjacent sites of the MPS, as illustrated in Fig. 3.14. For a spin system they are represented as follows:

$$\hat{S}_{l,l+1} = \sum_{\sigma_l\,\sigma_{l+1}\,\sigma_l',\sigma_{l+1}'} \delta_{\sigma_l,\sigma_{l+1}'}\,\delta_{\sigma_{l+1},\sigma_l'}\,|\sigma_l\,\sigma_{l+1}\rangle\,\langle\sigma_l'\,\sigma_{l+1}'|\,. \tag{3.47}$$
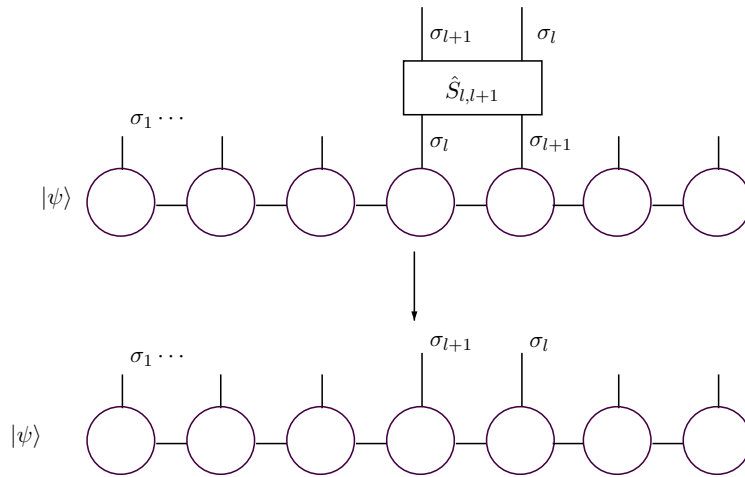
Figure 3.14: Action of a swap gate on an MPS.

Consider a Hamiltonian that includes the non-local interaction between sites i and j in the form of $e^{-i\hat{h}\tau}$, the procedure to time evolve the bond can be performed by first applying a set of swap gates so that the location of site j in the MPS is switched next to site i. Then, the local Trotter gate can be applied before moving site j back to its original position by another set of swap gates, as illustrated in Fig. 3.15.

$$\hat{S}_{i+1,i}\hat{S}_{i+2,i+1}\cdots\hat{S}_{j-1,j}e^{-i\hat{h}\tau}\hat{S}_{j,j-1}\cdots\hat{S}_{i+1,i+2}\hat{S}_{i,i+1}\,|\psi\rangle\,. \tag{3.48}$$
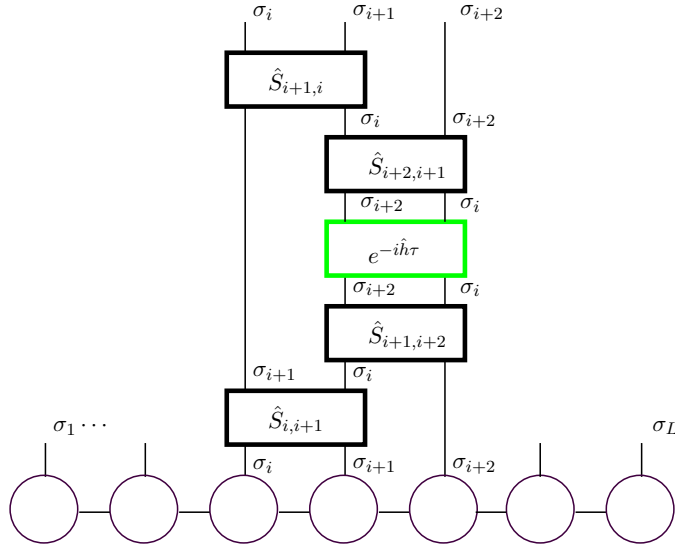
Figure 3.15: Diagrammatic representation of Eq. (3.48) of the case $j = i + 2$.

This simple scheme allows us to extend the employment range of the Suzuki-Trotter decomposition beyond nearest- neighbor Hamiltonians. The main disadvantage of this method is that it relies on the application of two-site operators which preserve the MPS form of the wave function only under the performance of an additional singular value decomposition (SVD) after every application [25]. If there is a great number of long-ranged interaction, the additional costs of these SVDs might pile up, rendering the swap gate approach inefficient.

3.6 Finite temperature calculations

Another important part of our project is the characterization of thermal effects on the spectrum of the spin ladder. In this chapter we will refrain from giving a complete description of the numerical methods used to produce these data. Instead, we give some introductory remarks and provide a more qualitative outline of the problem. For a more complete description we refer to Schollwöck's review [25].
We start by considering an arbitrary mixed state living in some space P spanned by the eigenvectors of a generic Hamiltonian $\hat{H}$. The state will be characterized by some density operator of the form (see Appendix 6.2):

$$\hat{\rho}_P = \sum_{a=1}^{d} s_a^2 \, |a\rangle_P \, \langle a|_P \, . \tag{3.49}$$

It is possible to express the thermal density matrix of a system within the MPS framework by means of purification [28]. To this end, we consider the density operator $\hat{\rho}_p$ as the partial trace over some auxiliary space A applied to a pure quantum state living in an enlarged Hilbert space $\mathcal{H}_{tot} = P \otimes A$. In mathematical terms:

$$|\psi\rangle = \sum_{a=1}^{d} s_a \, |a\rangle_P \, |a\rangle_A \Rightarrow \hat{\rho}_P = Tr_A(|\psi\rangle \, \langle\psi|) \, , \, \psi \in \mathcal{H}_{tot} \, . \tag{3.50}$$

As we introduce this new auxiliary space A, it is important to notice how it can be chosen arbitrarily since the Hamiltonian we are interested in only acts on the physical space P. Observing Eq. (3.49), the only restriction for the subspace A is the necessity for a matching dimension of P: it is convenient to simply take a copy of P. To setup the thermal density matrix $\hat{\rho}_\beta$ at some finite inverse temperature, we first express the operator as

$$\hat{\rho}_\beta = \frac{1}{Z(\beta)}e^{-\beta\hat{H}} = \frac{1}{Z(\beta)}e^{-\beta\hat{H}/2}\hat{I}e^{-\beta\hat{H}/2} \,. \tag{3.51}$$

The identity matrix can be interpreted as the density matrix of a quantum state with maximal entropy:

$$\hat{I} \;\propto\; \hat{\rho}_0 \Rightarrow \hat{\rho}_0 = diag(1/Z(0)\,, 1/Z(0)\,, \cdots\,, 1/Z(0))\,, \tag{3.52}$$

$$(3.52) \to (3.51) \Rightarrow \hat{\rho}_\beta \;=\; \frac{Z(0)}{Z(\beta)}e^{-\beta\hat{H}/2}\hat{\rho}_0 e^{-\beta\hat{H}/2}\,, \tag{3.53}$$

where $Z(0)$ denotes the partition function at infinite temperature.
If we now apply the mixed state purification to $\hat{\rho}_0$:

$$\hat{\rho}_\beta = \frac{Z(0)}{Z(\beta)}e^{-\beta\hat{H}/2}Tr_A(|\psi\rangle_0\,\langle\psi|_0)e^{-\beta\hat{H}/2} \,. \tag{3.54}$$

Since $\hat{H}$ only acts on subspace P, we can pull the thermal operators $e^{-\beta\hat{H}/2}$ inside the trace:

$$\hat{\rho}_\beta \;=\; \frac{Z(0)}{Z(\beta)}Tr_A(e^{-\beta\hat{H}/2}\,|\psi\rangle_0\,\langle\psi|_0\,e^{-\beta\hat{H}/2})\,, \tag{3.55}$$

$$\hat{\rho}_\beta \;=\; \frac{Z(0)}{Z(\beta)}Tr_A(|\psi\rangle_\beta\,\langle\psi|_\beta)\,,\; |\psi\rangle_\beta := e^{-\beta\hat{H}/2}\,|\psi\rangle_0 \,, \tag{3.56}$$

$$|\psi\rangle_0\,,\, |\psi\rangle_\beta \;\in\; \mathcal{H}_{tot}\,. \tag{3.57}$$

The thermal state $|\psi\rangle_\beta$ can be obtained by performing a standard MPS time evolution in imaginary time, using a Suzuki-Trotter decomposition analogous to the time evolution case:

$$e^{\beta\hat{H}} = \left(\prod_i^{L-1} e^{\hat{h}_i\kappa} + \mathcal{O}(\kappa^2)\right)^N\,,\; \kappa = \frac{\beta}{N}\,. \tag{3.58}$$

At this point we have all the necessary ingredients to retrieve the dynamic structure factor:

$$\langle\psi_T|\,\hat{S}^\beta_{l+L/2,m}(t_n)\hat{S}^\alpha_{L/2,m}\,|\psi_T\rangle \,. \tag{3.59}$$

Since all the steps have been discussed separately in the previous sections, we only include a diagrammatic representation of the procedure in Fig. 3.16.
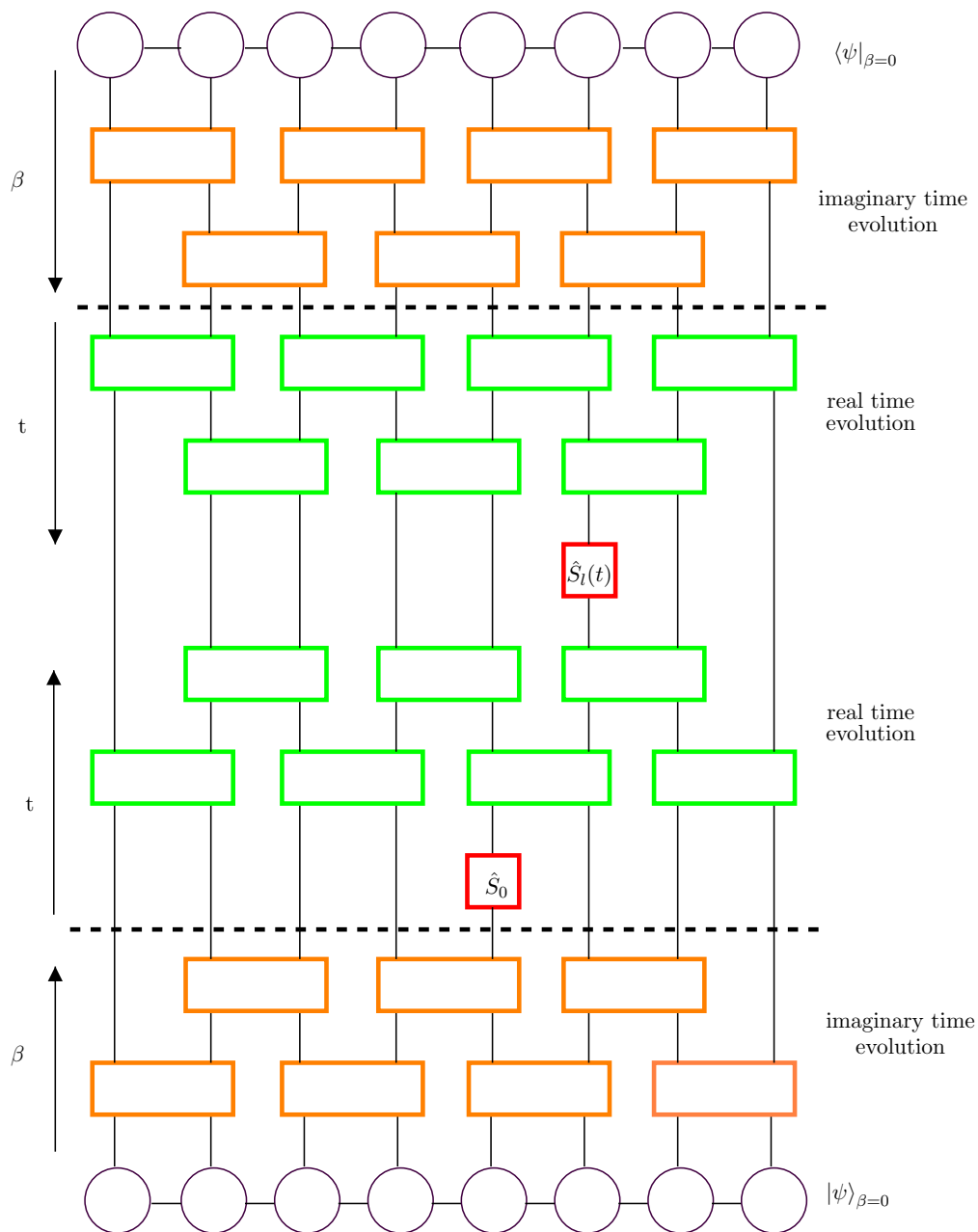
Figure 3.16: Diagrammatic representation of the dynamic structure factor at finite temperature of Eq. (3.59). The action of the swap-gates is not included for reasons of space.

4. Results

After having motivated the numerical background of this project, we now present the dynamic structure factor of the frustrated spin ladder obtained with tDMRG calculations. Following an introduction to the already known features of the spin ladder spectrum, we display results for the dynamic structure factor of the perfectly frustrated ladder at $T = 0$, managing to extract data in parameter configurations very close to the phase transition. In order to illustrate the effects of perfect frustration on the spectrum, we also present additional results for the spin ladder in a state of relaxed frustration. Moreover, we present the dynamic structure factor at finite temperature and discuss the details of thermal effects, finally motivating the anomalous spectral loss of the one triplet excitation in the vicinity of the phase transition.

4.1 Excitation and spectral features

Our numerical data examines the excitation spectrum of the spin ladder at different coupling regimes. As a preamble to the discussion of the results, we summarize some of the already known charachteristics of the spectrum which are discussed in great detail in Refs.[15] and [16].

- **Singlet phase:** The first excitation of the singlet phase consist in the flipping of a single spin, which results in the formation of a spin-triplet residing on the rung as illustrated in Fig.4.1
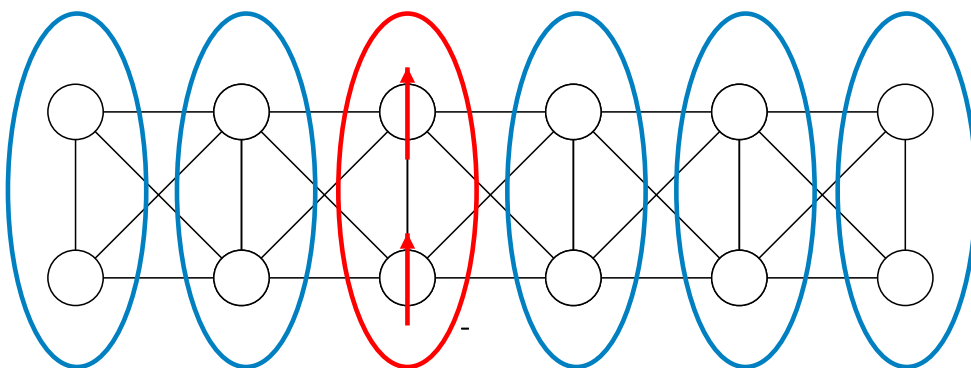
Figure 4.1: Red colored sites indicate a triplet excitation in singlet sites.

These excitations are known to be localized objects in the perfeclty frustrated regime $(J_\times = J_\parallel)$ [9] and thus do not exhibit dispersion in scattering simulations. Further high-energy excitations yield multi-triplet bound states. As an example, we illustrate the two-triplet excitation in Fig.4.2 :
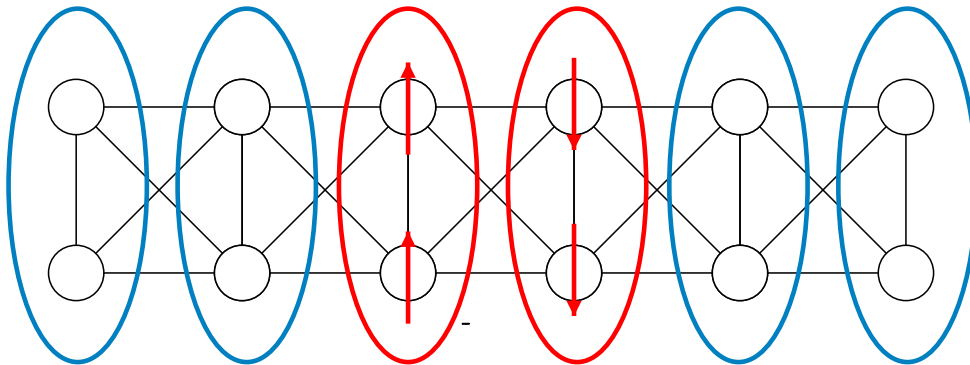
Figure 4.2: circled sites: 2 triplet excitations

In this phase, the behavior of the multi-triplet excitations can be understood by considering the system as a Haldane chain [36, 22, p. 24] with open boundary conditions. The length of the chain is determined by the number of adjacent triplet rungs of the excitation. In the case of Fig. 4.2, for instance, the length of the corresponding Haldane chain is two and exact diagonalization yields the following energies:

$$\frac{E_{2s}}{J_\parallel} = 2(j'-1)\,, \frac{E_{2t}}{J_\parallel} = 2j'-1\,, \frac{E_{2q}}{J_\parallel} = 2j'+1\,, \tag{4.1}$$

$$j' \equiv \frac{J_\perp}{J_\parallel}\,. \tag{4.2}$$

In this context, these values represent the energies of the two-triplet excitation in the frustrated spin ladder. The same procedure can be applied to further multi-triplet excitations. The key aspect of these energies lies in the j' dependency: in fact, as we approach the critical value of the coupling parameters, these energies converge toward energies far below the one-triplet excitation. However, these excitations are not directly accessible at $T = 0$ because pure spin-spin interaction (in absence of thermal fluctuations) in the perfectly frustrated regime $J_\parallel = J_\times$, prevents them from arising [15]. In the presence of finite temperature though, the competing effects of thermal fluctuations generates a non vanishing spectral weight of these multi-triplet modes. As we approach the critical point, large numbers of these states start to appear below the one-triplet excitation: this great variety of low lying energy states plays a key role in understanding the spectral weight redistribution of the one-triplet band displayed in the figures of Section 4.3.

- **Triplet phase** As mentioned in Section 2.2, the ground state of the rung triplet phase forms a total spin singlet $S = 0$. The first excited state in this phase forms a total spin triplet $S = 1$, also known as the dispersive one magnon excitation [2, pp. 704-706], corresponding to flipping the spins of two sites of a rung, as displayed in Fig. 4.3.
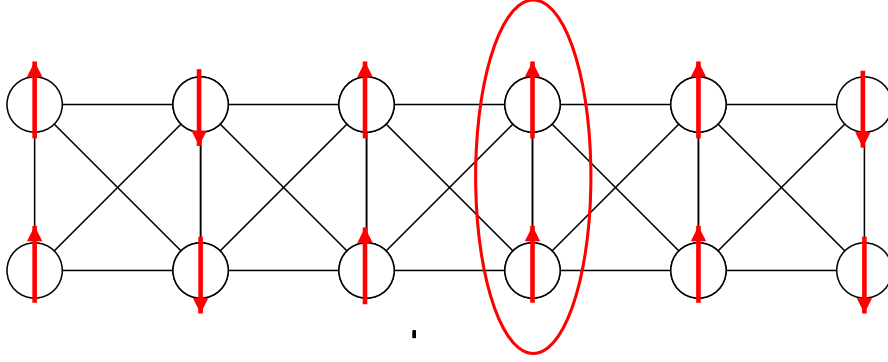
Figure 4.3: Circled rung corresponds to one magnon excitation.

In the thermodynamic limit, the first excitation is energetically separated from the ground state by a gap $\Delta \approx 0.4105 J_\parallel$. Further excitations are referred to as multi-magnon bands [34] and arise at integer multiples of the one-magnon gap: e.g the two-magnon band arises at $\Delta_2 = 2\Delta$. It should be noted, however, that the location of these energy values is strongly dependent upon the actual size of the system. Other excitations in the rung-triplet phase correspond to the formation of a rung singlet as a consequence of a spin-flip at a single site, as illustrated in Fig. 4.4.
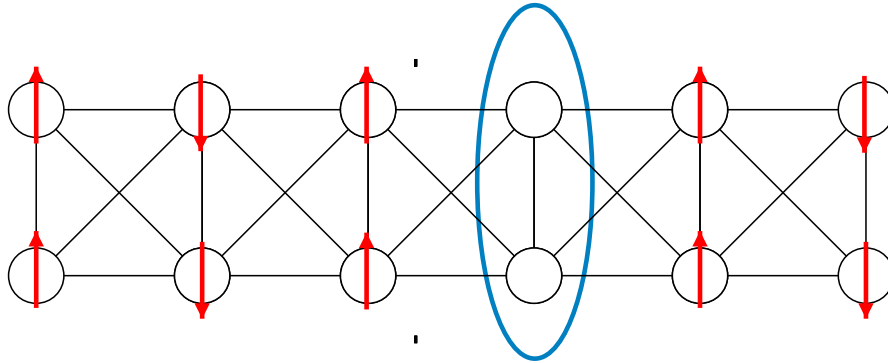
Figure 4.4: The blue circle corresponds to a singlet excitation.

These excited states are localized and thus do not experience spectral dispersion. As shown in Ref. [16], these energy levels experience a size related convergence toward the value $E/J_\parallel \approx 1.208$, which lies in the vicinity of the one-magnon gap Δ.

4.2   Zero-temperature spectra

In a first study, we focus on the spectral feature of the spin ladder at zero temperatures. In particular, we examine these dynamical features at values around the quantum critical point and perfect frustration,

$$J_\times = J_\parallel = 1 \, , \, J_{\perp,c} = 1.401 \, . \tag{4.3}$$

We fix $J_\times = J_\parallel = 1$, and tune the rung coupling $J_\perp$ to probe the different phases of the spin ladder. We initialize the MPS as a Néel state as starting wave function for the DMRG algorithm. In this parameter regime however, we noticed that DMRG has trouble identifying the correct ground state, as illustrated by the staggered magnetization displayed in Fig. 4.5.
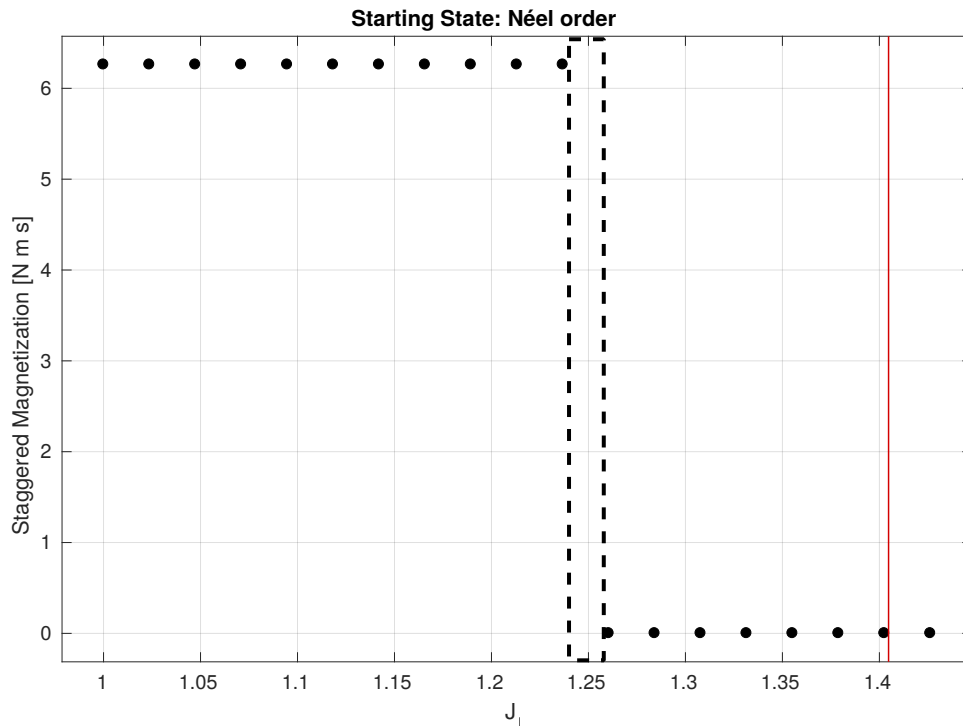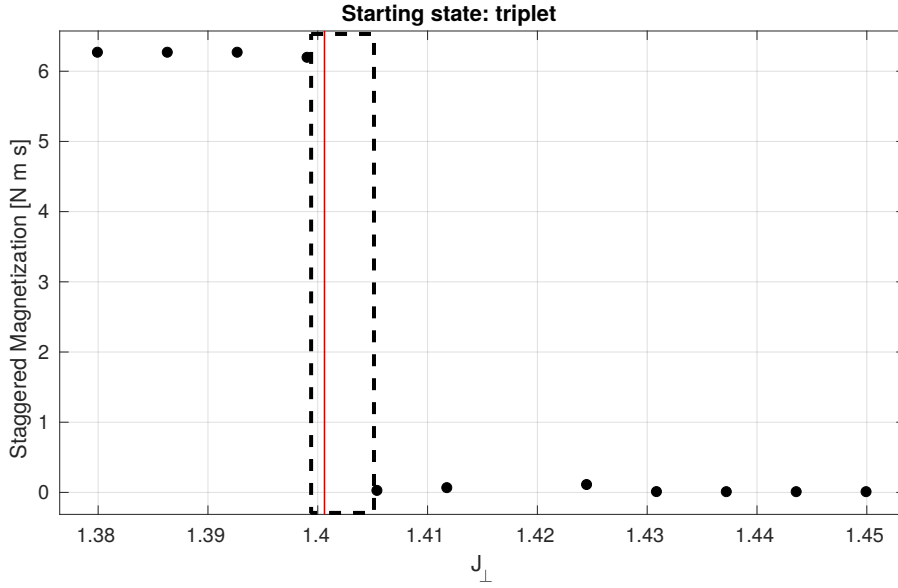
Figure 4.5: Staggered magnetization (see Eq. (2.9)) of the ground states calculated with DMRG using a Néel state as starting wave function.

As discussed in Section 2.2, the staggered magnetization is the order parameter of the frustrated ladder. The phase transition seems to be located around $J_\perp = 1.25$, in disagreement with the results of other publications [30, 15]. This deviation can be attributed to several issues of the finite-size DMRG:

- The initial state provided for the DMRG algorithm is of Néel order on all $J_\perp$ bonds. Due to its magnetic order, this state has a slight bias to the ground state of the singlet phase ($J_\perp \gg J_\parallel, J_\times$).

- In addition, the singlet state seems to be a rather persistent local energy minimum also in the triplet phase. With DMRG performing only updates on two sites at once, the algorithm shows great difficulties to converge to the actual triplet ground state only allowing for local updates. Note that we also tried converging the state using an initial noise term [32] in the DMRG. This did not yield better convergence.

In order to solve the convergence issue, it is useful to change the initial state of the algorithm to a rung-antiferromagnetic state with similar to the one shown in Fig. 2.10. The DMRG with this initial state yields a phase transition value of $J_\perp$ in good agreement with previous results, as illustrated by the values of the staggered magnetization shown in Fig. 4.6

Figure 4.6: Staggered magnetization (see Eq. (2.9)) of the ground states calculated with DMRG using a rung-antiferromagnetic state as starting wave function.

At this point we can compute the dynamical structure factor of the spin-ladder and consequently the spectrum. In the following we present the dynamic structure factor for chain size 100×2 and the $J_\perp$ parameter ranging from 1.2 (Fig. 4.7) to 1.8 (Fig. 4.10). The symmetric channel ($k_y = 0$) results are portrayed on the left of each panel, the antisymmetric ($k_y = \pi$) on the right. Other DMRG tuning parameters are a cutoff value of e^{-9} (discarded weight), a line broadening parameter of $\eta = 0.1$ and a time limit of $T = 40s$. The maximal time T_{max} achieved by tDMRG is reported in each figure separately.
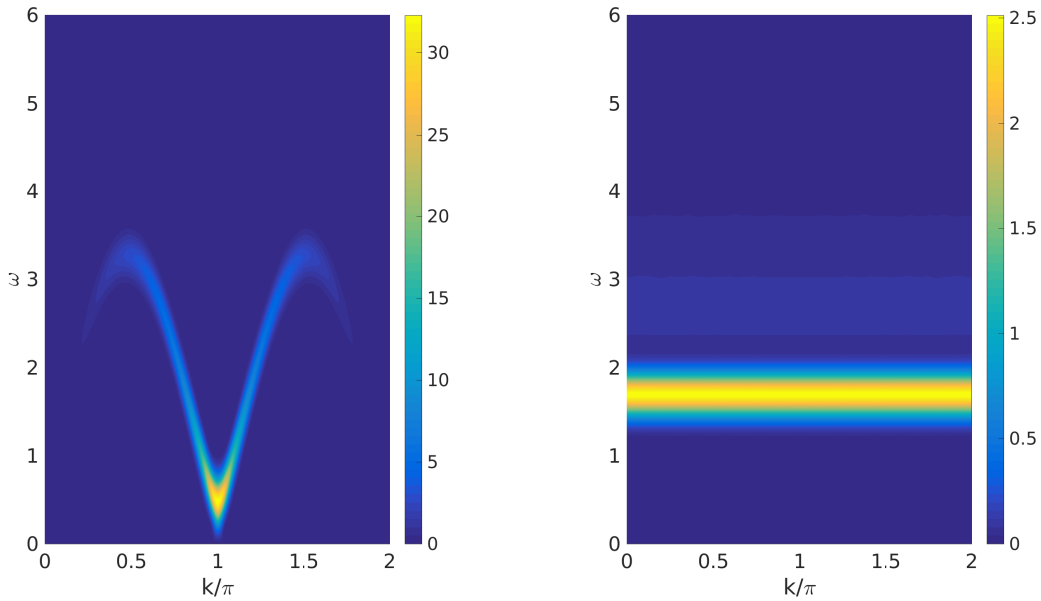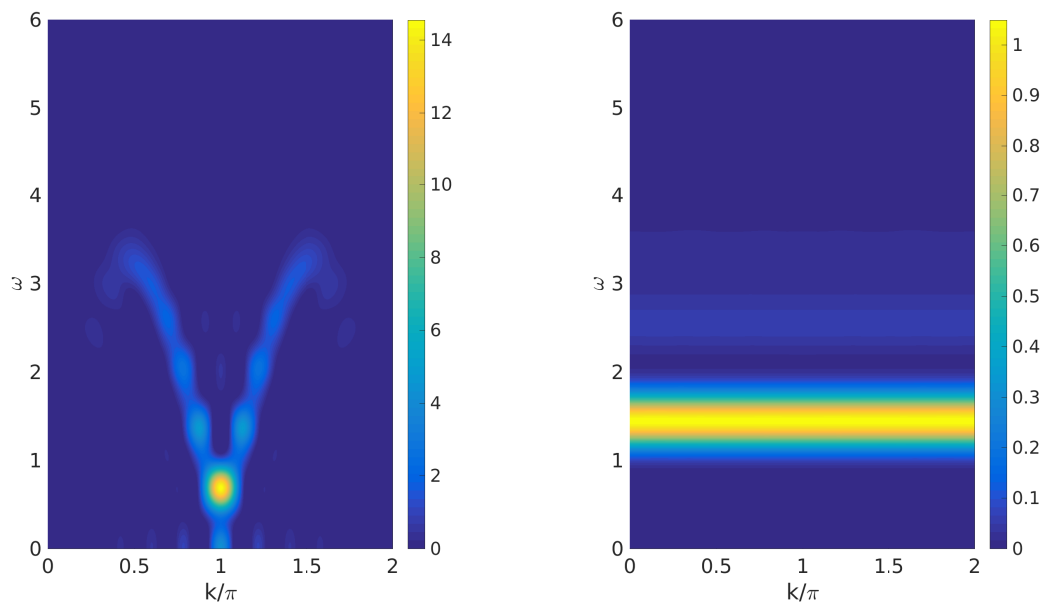

Figure 4.7: $J_\perp = 1.2$, $J_\parallel = J_\times = 1$, $T_{max} = 40\,s$
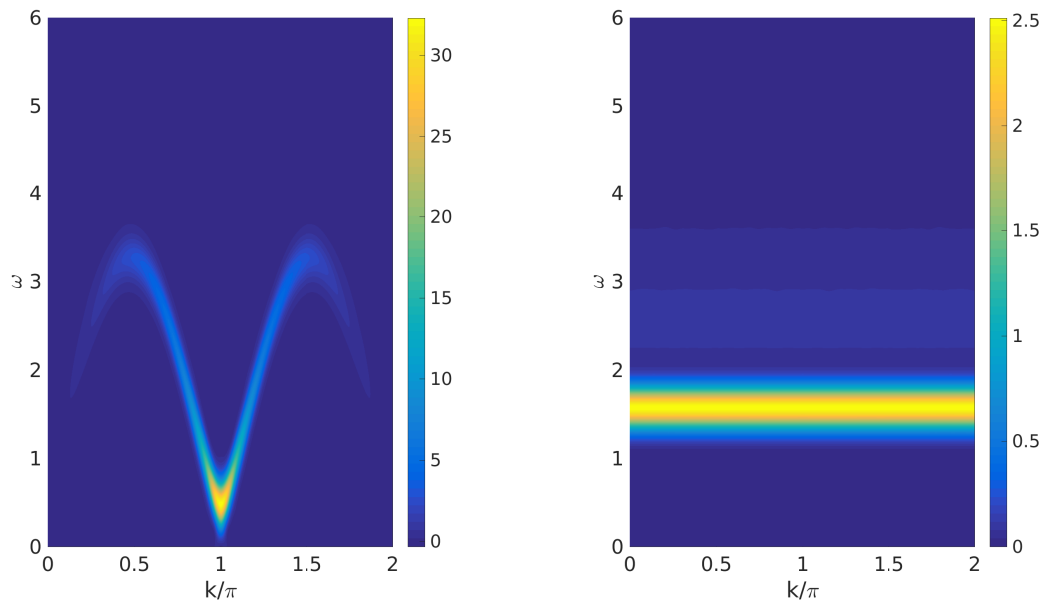
Figure 4.8: $J_\perp = 1.3\,,\, J_\parallel = J_\times = 1\,,\, T_{max} = 40\,s$
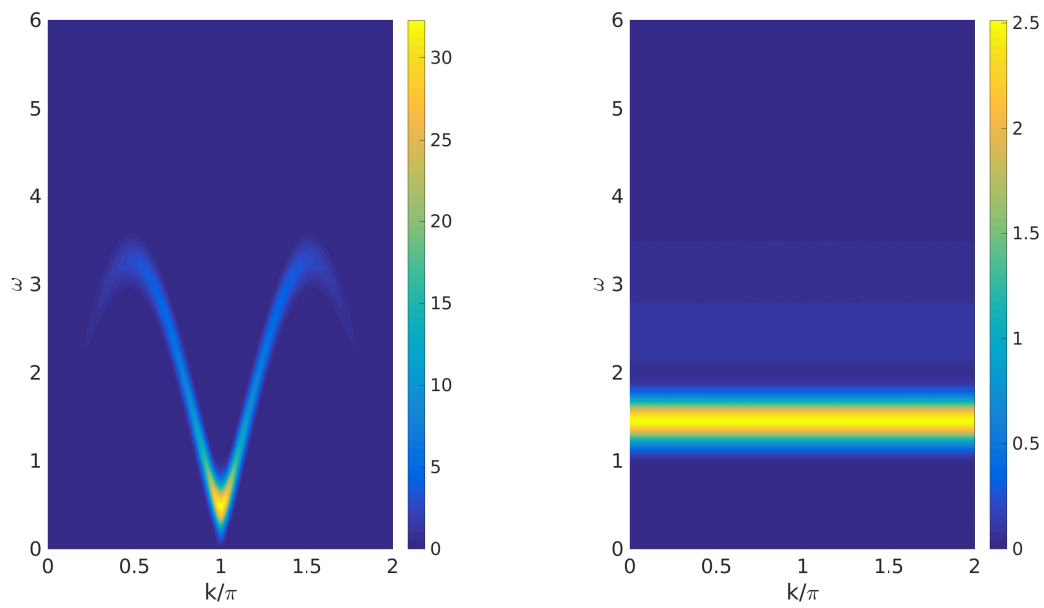
Figure 4.9: $J_\perp = 1.4\,,\, J_\parallel = J_\times = 1\,,\, T_{max} = 40\,s$
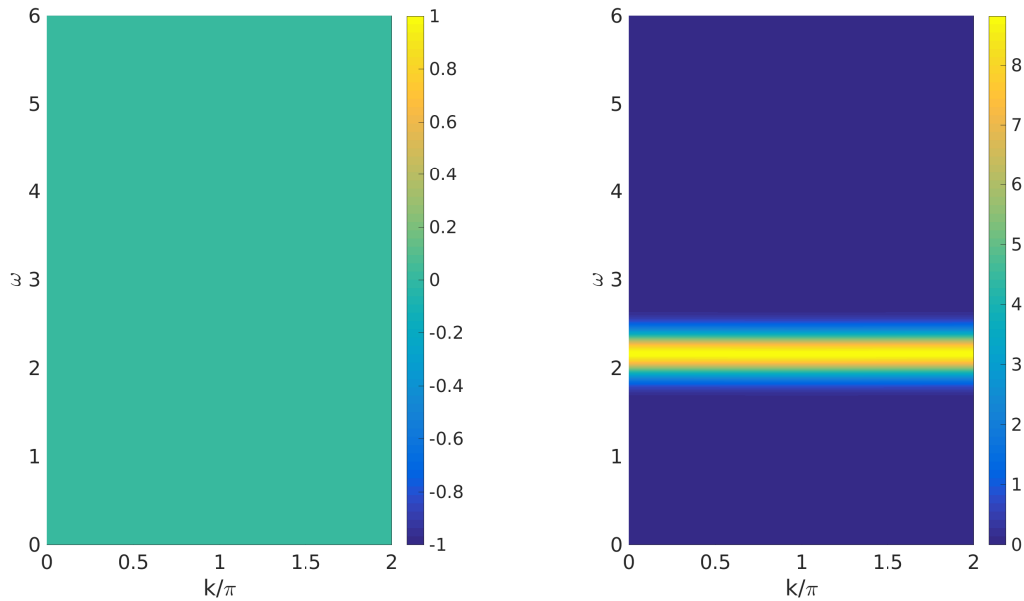
Figure 4.10: $J_\perp = 1.8$, $J_\parallel = J_\times = 1$, $T_{max} = 40\,s$

In this parameter regime (Figs. 4.7-4.10), a typical DMRG ground state search required a bond dimension of $D \approx 150$ and $D \approx 200$ at maximum time step T_{max}.

For $J_\perp < J_{\perp,c}$ in Figs. 4.7-4.9 (rung triplet ground state), we notice dispersion in the symmetric channel which can be directly related to the one-magnon excitation of a Haldane chain [34]. The antisymmetric channel exhibits the discrete one-singlet excitation as a completely flat spectral feature (Fig. 4.10).

For $J_\perp > J_{\perp,c}$ in Fig. 4.10 (rung singlet ground state), we notice the localized one-triplet excitation in the antisymmetric channel and no spectral features at all in the symmetric channel.

The important aspect that should be stressed, is the tendency of the first excited state (portrayed as the bright yellow line appearing in the antisymmetric channel) to move toward smaller values as we approach the critical point $J_\perp \to 1.401$ and then increasing again, as we further increment the $J_\perp$ values (see Figs. 4.7-4.10). With L=100, the DMRG converges very slowly in the vicinity of the phase transition due to the appearance of many low-energy excitations (see Section 4.1). To this end, we reduce the system length L from 100 to 40, allowing us to decrease the computational costs and study regimes very close the the phase transition. Apart from reducing the system length, the other calculation parameters were left unvaried:

- cutoff value e^{-9} (discarded weight)
- line broadening parameter of $\eta = 0.1$
- time limit of $T = 40s$
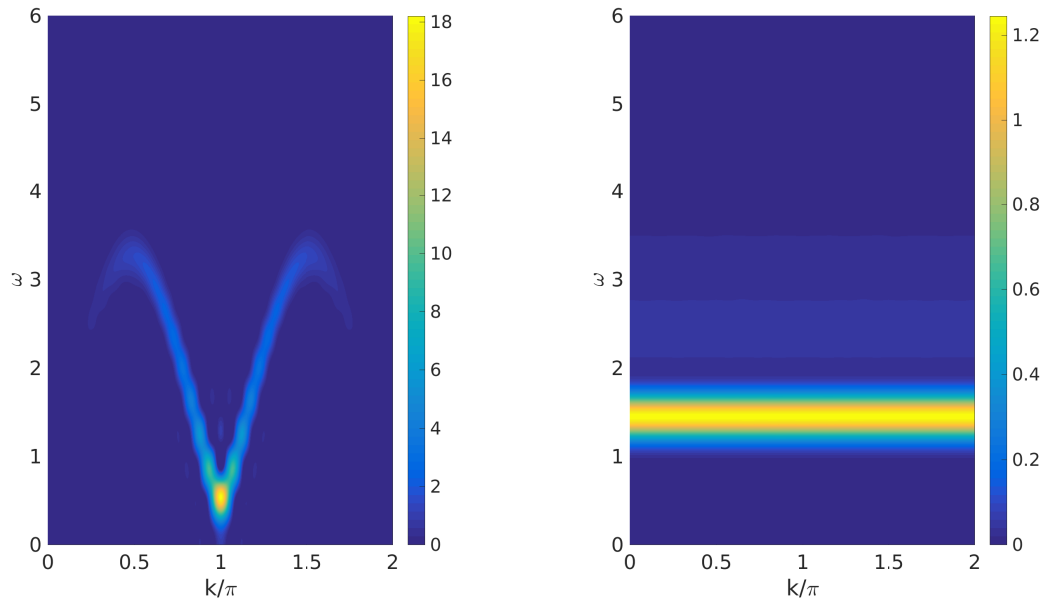
Figure 4.11: $J_\perp = 1.402\,,\ J_\| = J_\times = 1\,,\ T_{max} = 40\,s$

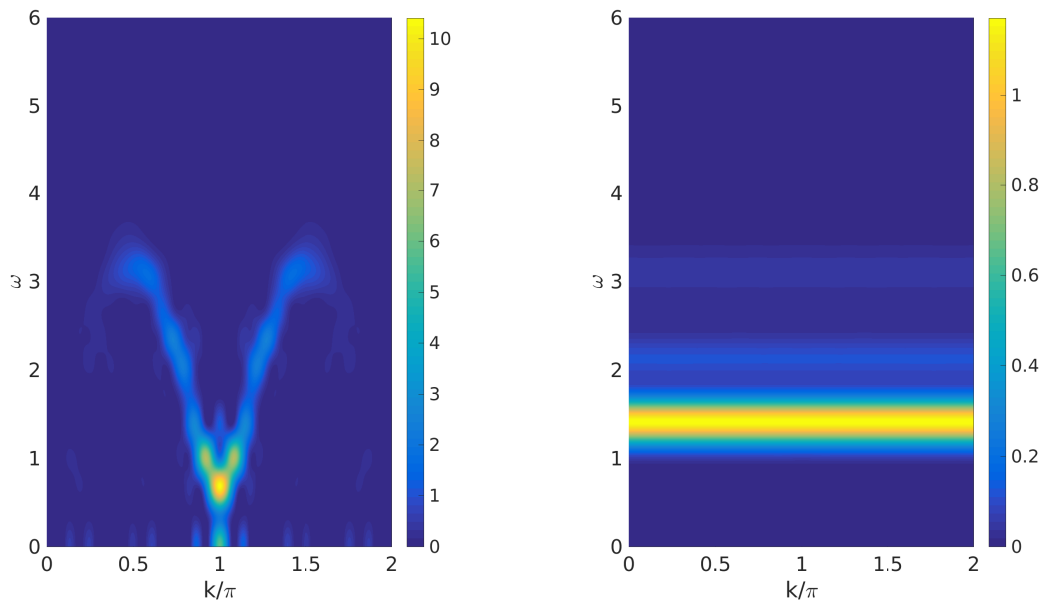**Figure 4.12:** $J_\perp = 1.405\,,\ J_\| = J_\times = 1\,,\ T_{max} = 40\,s$

Figure 4.13: $J_\perp = 1.406$, $J_\parallel = J_\times = 1$, $T_{max} = 40\,s$

It should be noted that the coupling parameter combination responsible for the phase transition is susceptible to the size of the system. Therefore we find the characteristic one-magnon dispersion even at values $J_\perp > 1.401$. The striking feature is the vanishing of the spectral gap which can be observed in Fig. 4.13. This indicates that the phase transition is slightly shifted to $J_\perp \approx 1.406$, where the gap closes completely, signaling the divergence of correlation length. In this regime (Figs. 4.11-4.13), our calculations required a bond dimension $D \approx 200$ at the maximum time step T_{max} and $D \approx 150$ for the ground-state search.

4.2.1   Relaxed frustration regime

In order to show the role of frustration in this particular system, we include the dynamic structure factor of the ladder in a relaxed frustration regime: i.e at $J_\perp = J_\parallel = 1$. In this region of the phase diagram, the critical point is located at $J_\times = 0.599$ [16]. We present simulation results for $J_\times$ ranging from 0.4 (Fig. 4.14- rung triplet phase) to 0.7 (Fig. 4.17- rung singlet phase). The calculations are once again performed on a ladder length of $L = 100$ and the numerical parameters are left unvaried:

- cutoff value e^{-9} (discarded weight)
- line broadening parameter $\eta = 0.1$
- time limit $T = 40s$

as in the fully frustrated case, the symmetric channel ($k_y = 0$) is displayed on the left panels, the antisymmetric channel ($k_y = \pi$) on the right.
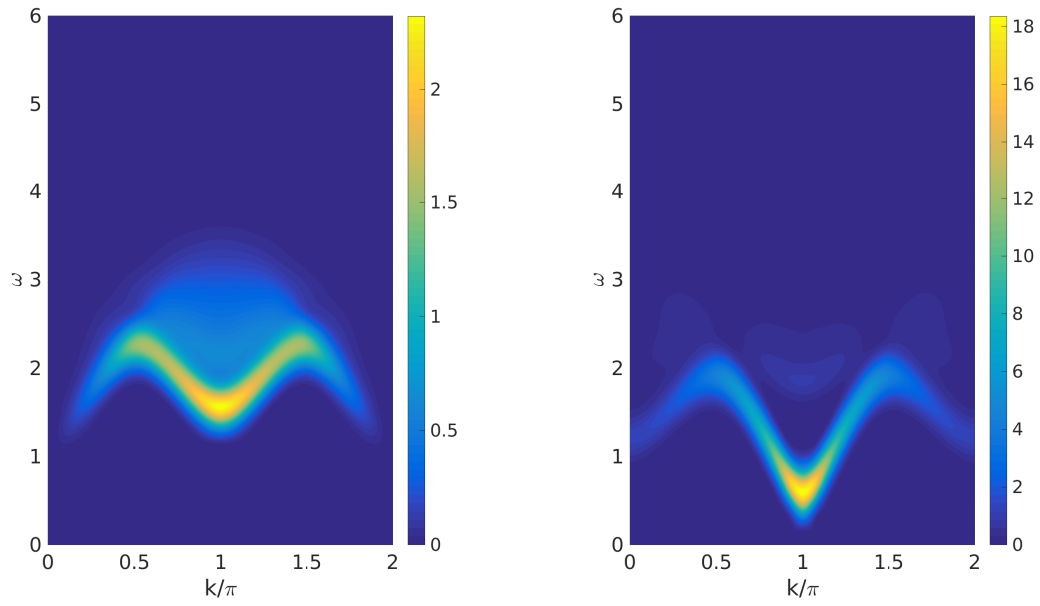
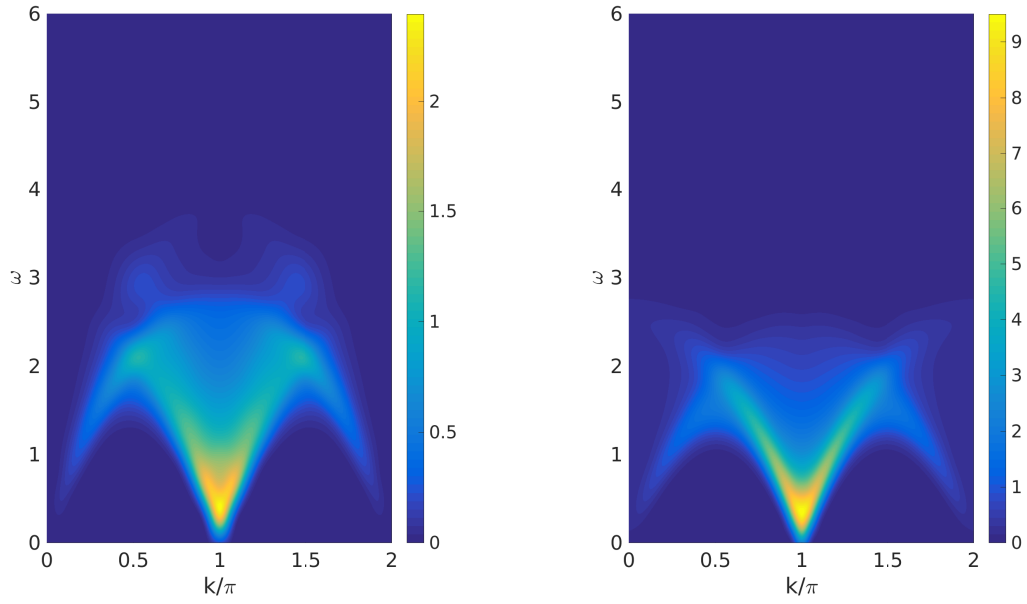**Figure 4.14:** $J_\times = 0.4$, $J_\perp = J_\parallel = 1$, $T_{max} = 40\,s$
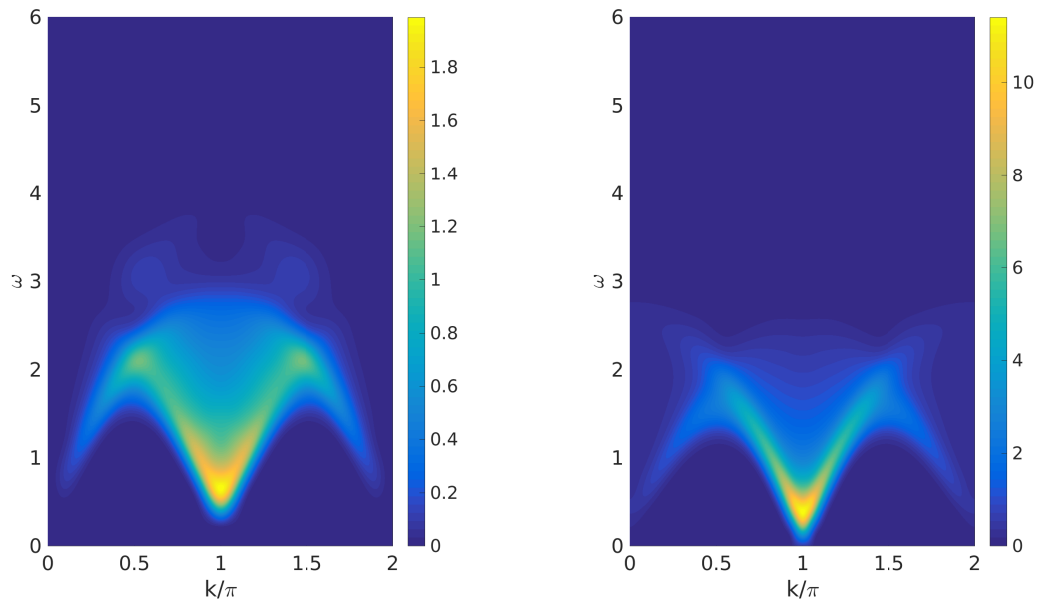
Figure 4.15: $J_\times = 0.58$, $J_\perp = J_\parallel = 1$, $T_{max} = 38.3\,s$

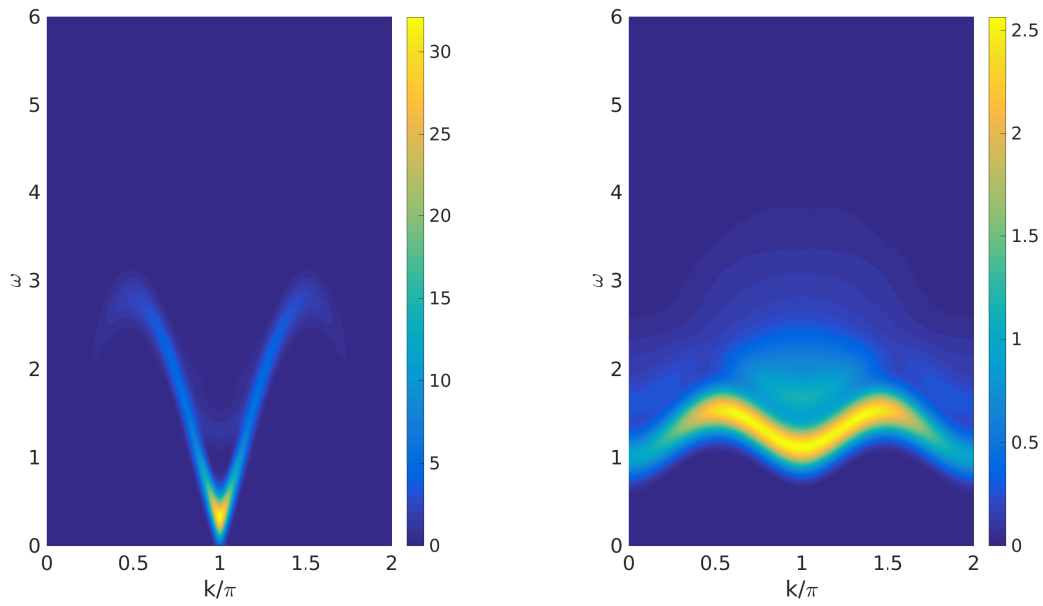**Figure 4.16:** $J_\times = 0.6\,,\ J_\perp = J_\parallel = 1\,,\ T_{max} = 24.9\,s$

Figure 4.17: $J_\times = 0.7\,,\ J_\perp = J_\parallel = 1\,,\ T_{max} = 40\,s$

The required bond dimension increases significantly as we approach criticality (Figs. 4.15-4.16), varying from $D \approx 100$ to $D \approx 350$ for the ground state search and from $D \approx 300$ to $D > 3000$ at maximum time step T_{max}.

The important aspect that should be noted, is how the one-triplet excitation appearing in the antisymmetric channel now appears to have dispersive features (right panel of Figs. 4.14-4.17) in contrast to the results shown for perfect frustration $J_\times = J_\parallel = 1$ above (right

panel of Figs. 4.7-4.10). The consequence of perfect frustration appears to be the complete localization of the single- and multi-triplet excitations. Again, we observe that the spectral gap closes towards the critical point. In contrast to the perfectly frustrated spin ladder, we notice that the gap closes in both channels (Fig. 4.16). This interesting property could be a consequence of relaxed frustration. As mentioned in Ref. [15], multi-triplet bound states are not accessible at $T = 0$ in the perfectly frustrated regime. By relaxing the frustration, we may indeed be able to probe them directly and witness the closing of the spectral gap.

4.3 Finite temperature

As observed in the $T = 0$ data for the rung-singlet phase, no direct coupling to the multi-triplet bound states is possible as a consequence of perfect frustration [15]. The only visible spectral features are the one-triplet excitation in the antisymmetric channel (left panel of Figs. 4.7-4.10). In the following, we select some of the previously calculated $T = 0$ spectra and show how finite temperature yields a spectral weight redistribution involving multi-triplet bound states. In order to show the onset of these excitations, we start from low temperatures, gradually increasing them until we reach energies comparable with the first excitation in the antisymmetric channel. Obtaining reliable results for the high-temperature regimes is not always possible in the mixed state purification framework as entanglement growth during real-time evolution is significantly increased by thermal fluctuations. At large temperatures, we typically have difficulties to perform the real-time evolution to larger time scales ($T_{max} < 10$). This results in a poor frequency resolution and prevents us from drawing conclusions from the data.

In the following, we present the spectra of the spin ladder in the perfectly frustrated regime $J_\times = J_\parallel = 1$ with $J_\perp$ ranging from 1.3 (Figs. 4.18-4.20) to 1.8 (Figs. 4.24-4.26). In order to facilitate the calculations and access longer times, we reduced the system length from $L = 100$ to $L = 50$. The other numerical parameters are:

- Cutoff value e^{-9} (discarded weight)
- Line broadening parameter $\eta = 0.1$
- Time limit $T = 80\,s$

It should be noted that the line broadening parameter plays a less relevant role in the finite-temperature calculations as thermal effects already mitigate some of the finite-time effects present in the Fourier transform of Eq. (3.12). For reasons of consistency we used a line broadening parameter of $\eta = 0.1$. The maximally reached time with tDMRG is reported separately in every figure.

The effects of finite temperatures are also recognizable from the increased bond dimensions of the treated quantum states: a thermal state typically requires a bond dimension $D \approx 100$ initially and $D > 3000$ at maximum time T_{max}.

As before, the symmetric channel ($k_y = 0$) is displayed on the left panels and the antisymmetric channel ($k_y = \pi$) on the right.
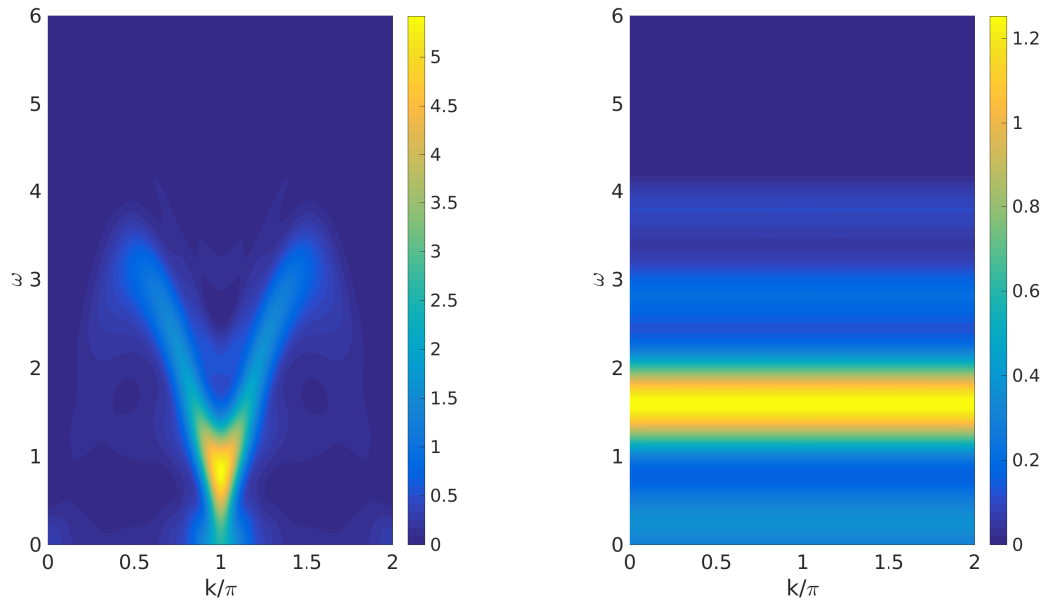
4.3.1   Rung triplet phase:

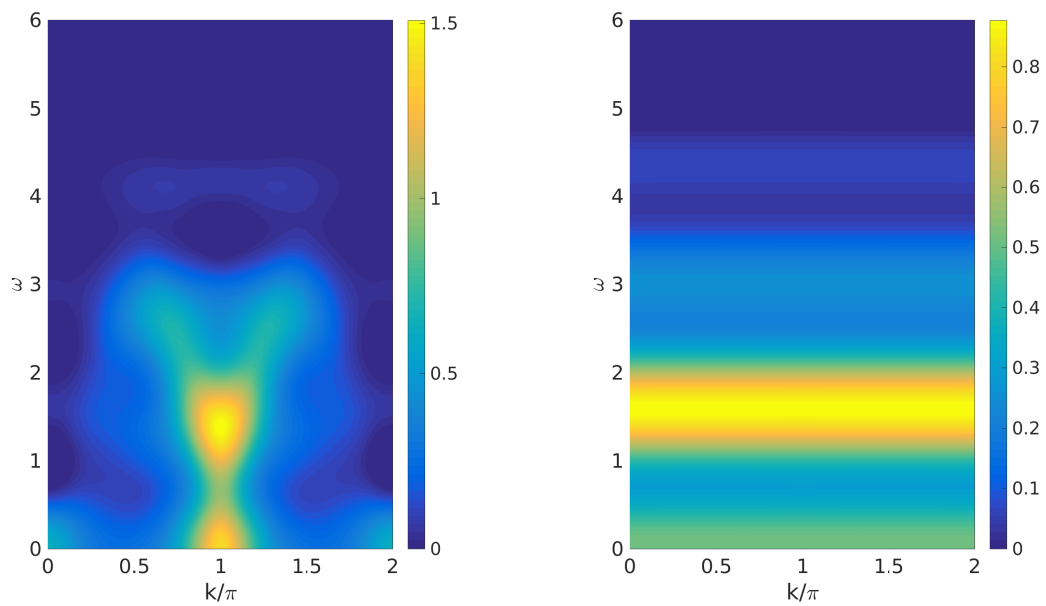**Figure 4.18:** $J_\perp = 1.3\,,\ J_\parallel = J_\times = 1\,,\ \beta = 3\,,\ T_{max} = 7.55\,s$

Figure 4.19: $J_\perp = 1.3\,,\ J_\parallel = J_\times = 1\,,\ \beta = 1.5\,,\ T_{max} = 5.75\,s$
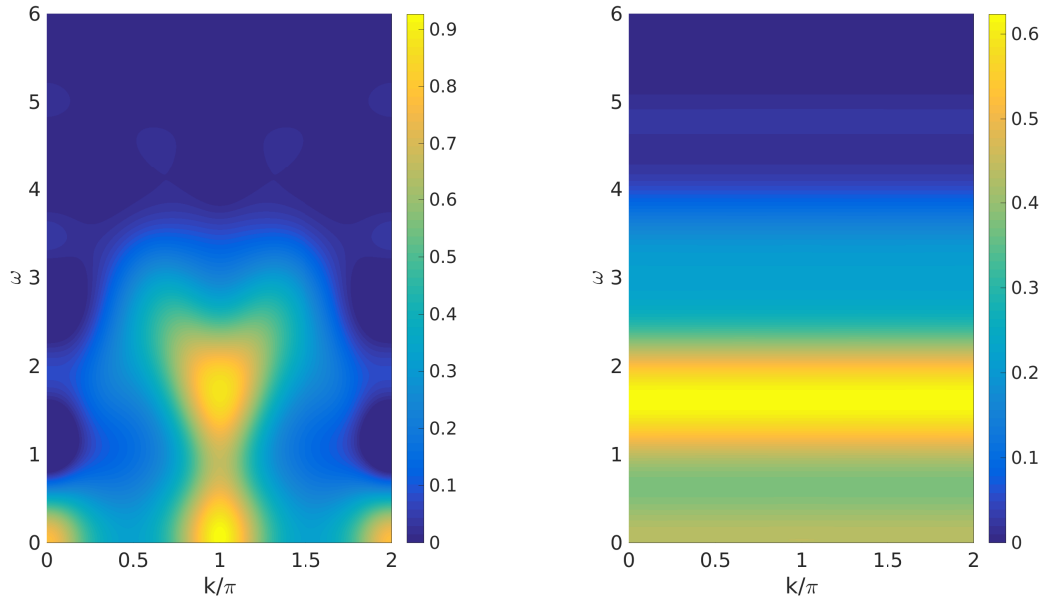
Figure 4.20: $J_\perp = 1.3$, $J_\parallel = J_\times = 1$, $\beta = 1$, $T_{max} = 4.85\,s$

4.3.2   Rung singlet phase:

Bringing finite temperatures into play, the actual size system starts playing a very important role. Our goal is to observe the onset of multi-triplet bound states while approaching the critical point from the side of the singlet phase. These bound states are extended objects, meaning their number is proportional to the number of available rungs, therefore, finite size effects become very noticeable as seen by comparing our results ($L_{max} = 50$) with those produced by Honecker et al. [15] ($L_{max} = 16$). As an example, comparing the right panel of Fig. 3 in Ref. [15] with Fig. 4.24-4.26 reveals how the new thermally induced bands occur at slightly shifted energy values. Furthermore, the spectral weight decrease in Fig. 4.26 is already similar to the one shown in Fig. 3 of Ref. [15], despite the temperature used here ($\beta = 1$) is still relatively far from compensating the energetic gap of Fig. 4.10 ($\beta \approx 0.5$). We speculate that the extended size of the ladder provides a wider array of multi-triplet bound states to fuel the spectral weight decrease of the one-triplet excitation, but a definitive confirmation of this statement is not possible as it would require direct access to the numerical results obtained in Ref. [15].
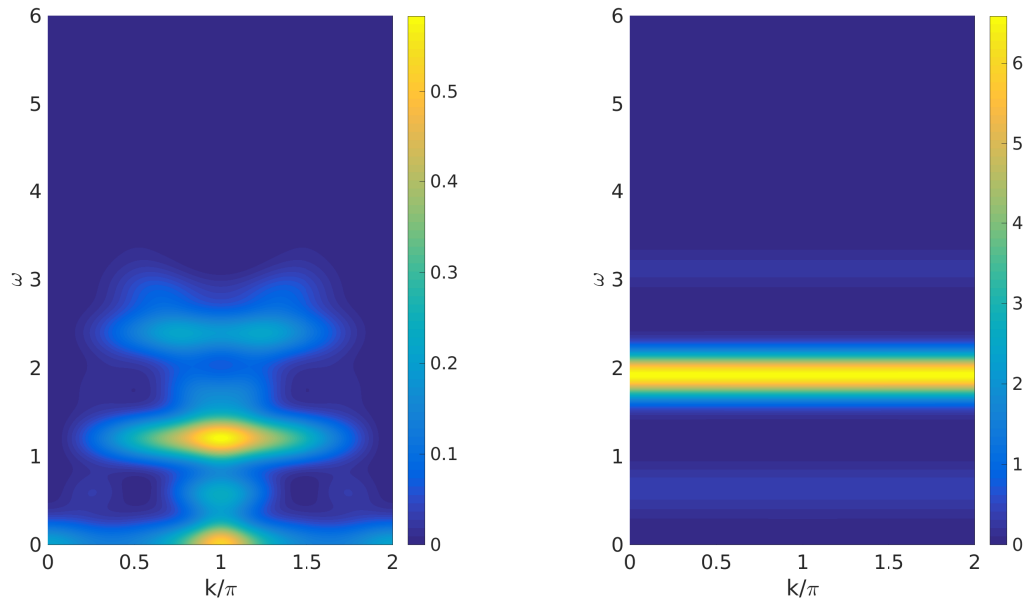
Figure 4.21: $J_\perp = 1.6$, $J_\parallel = J_\times = 1$, $\beta = 3$, $T_{max} = 80\,s$
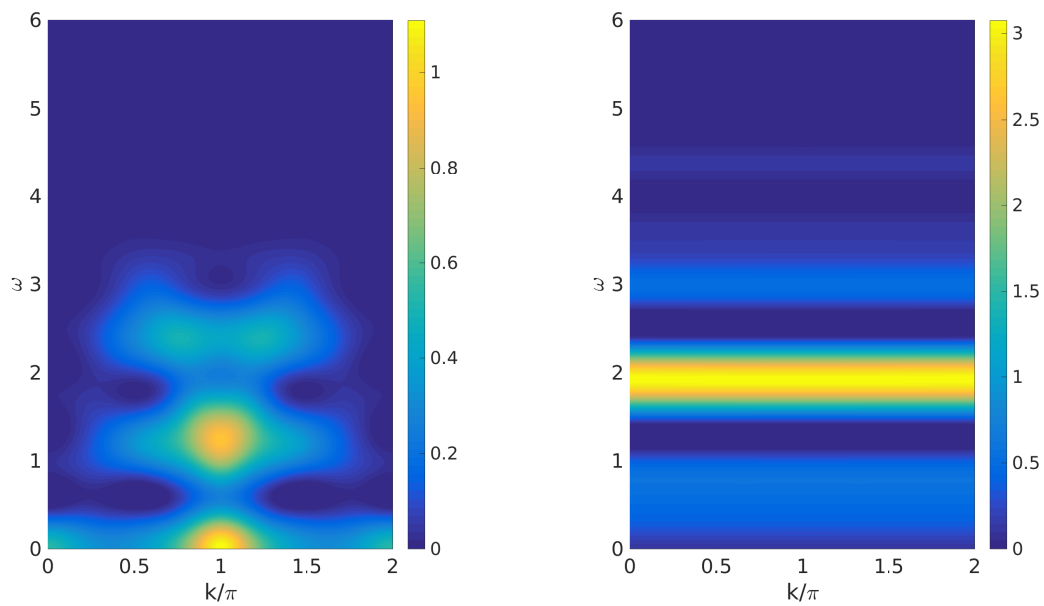

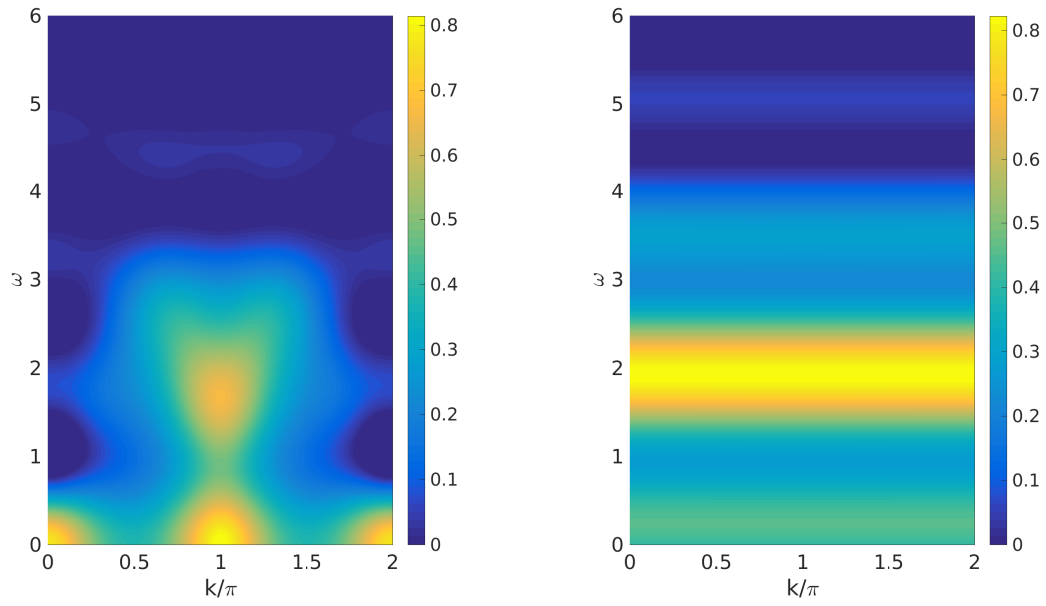**Figure 4.22:** $J_\perp = 1.6$, $J_\parallel = J_\times = 1$, $\beta = 2$, $T_{max} = 80\,s$

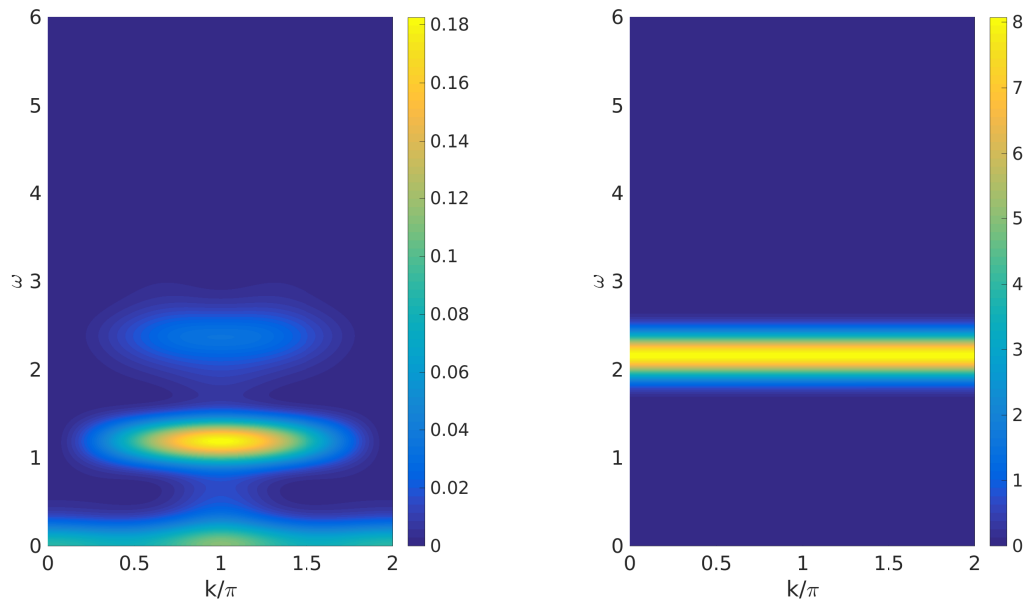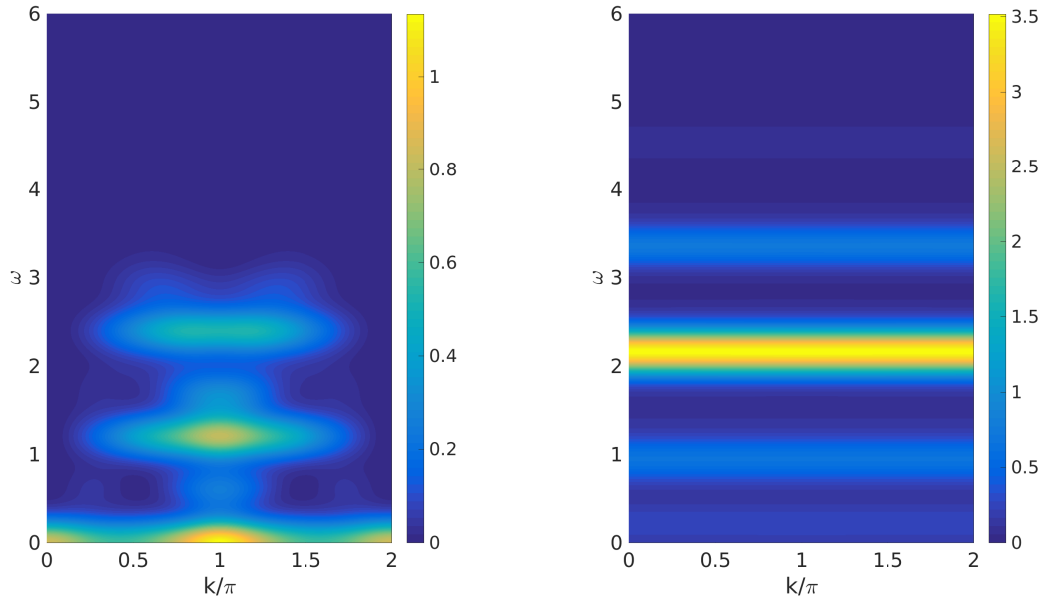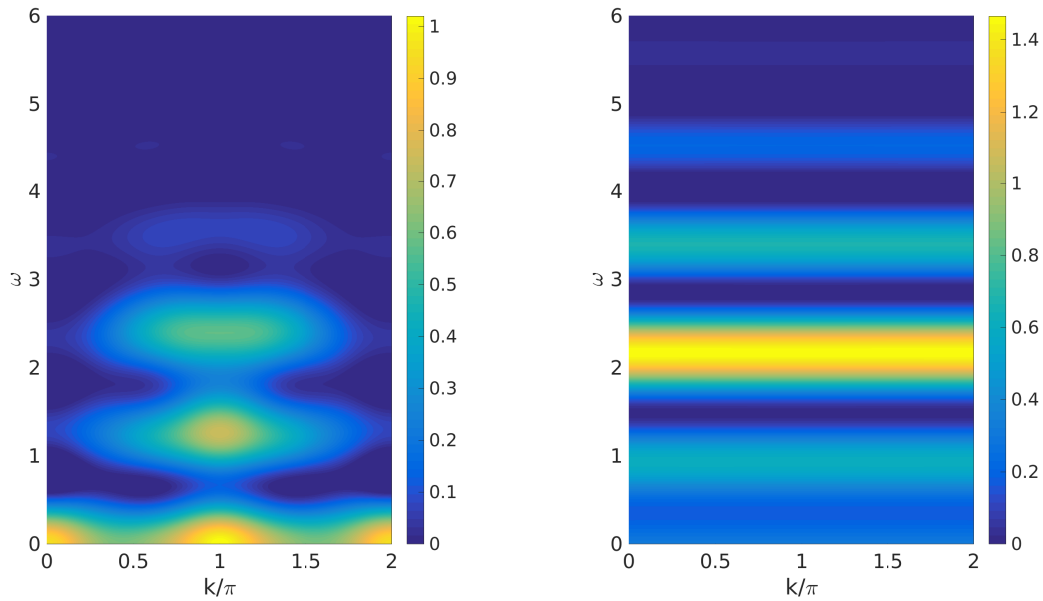**Figure 4.23:** $J_\perp = 1.6$, $J_\parallel = J_\times = 1$, $\beta = 1$, $T_{max} = 5.9\,s$

Figure 4.24: $J_\perp = 1.8$, $J_\parallel = J_\times = 1$, $\beta = 3$, $T_{max} = 80\,s$

Figure 4.25: $J_\perp = 1.8$, $J_\| = J_\times = 1$, $\beta = 1.5$, $T_{max} = 5.3\,s$

Figure 4.26: $J_\perp = 1.8$, $J_\| = J_\times = 1$, $\beta = 1$, $T_{max} = 4.45\,s$

The spectral weight redistribution in the anti-symmetric channel of Figs. 4.21-4.26 appears evident. As we approach high temperatures, we notice how the one-triplet excitation loses spectral weight appreciably in favor of the onset of new non dispersive spectral feature both above and below it. These bands correspond to the aforementioned multi-triplet bound states, which are now accessible due to the interference of thermal fluctuations.

4.3.3   Vicinity of the phase transition:

In the vicinity of the phase transition, we attempt to capture the influence of finite temperatures both coming from the rung triplet and rung singlet phase:
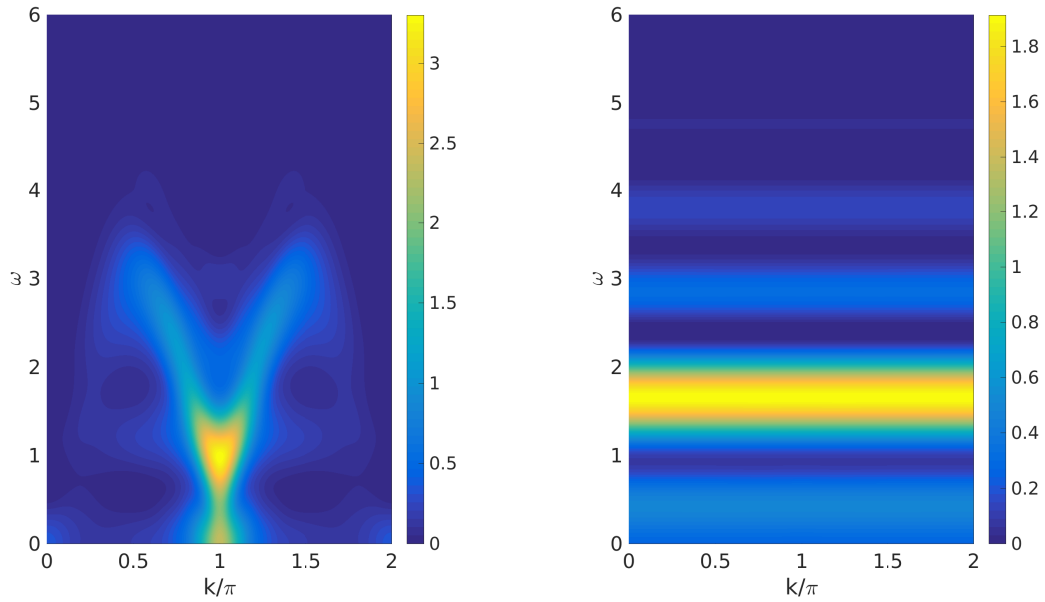

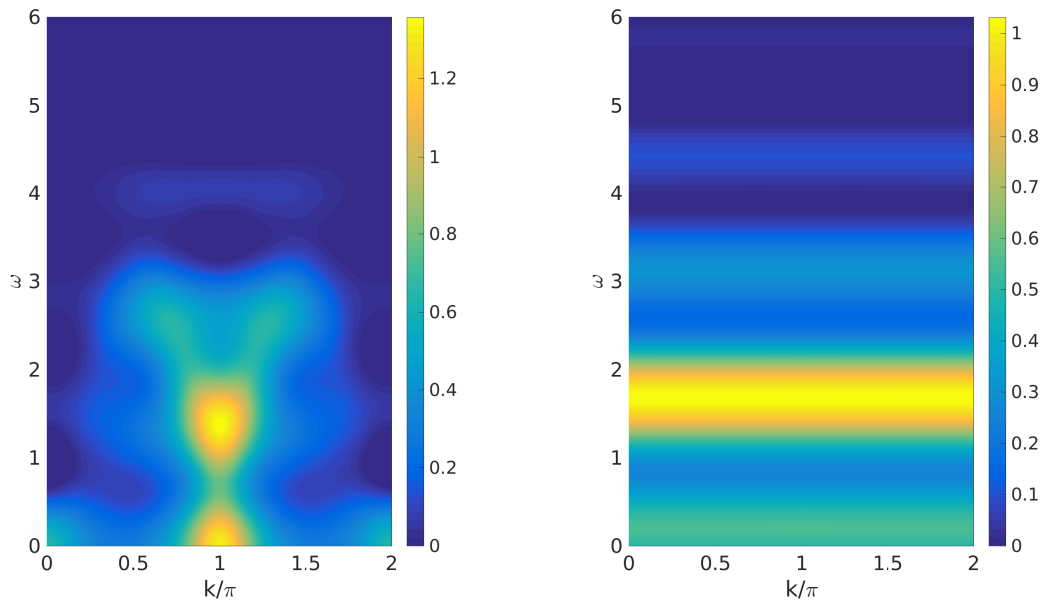**Figure 4.27:** $J_\perp = 1.38$, $J_\parallel = J_\times = 1$, $\beta = 3$, $T_{max} = 7.9\,s$

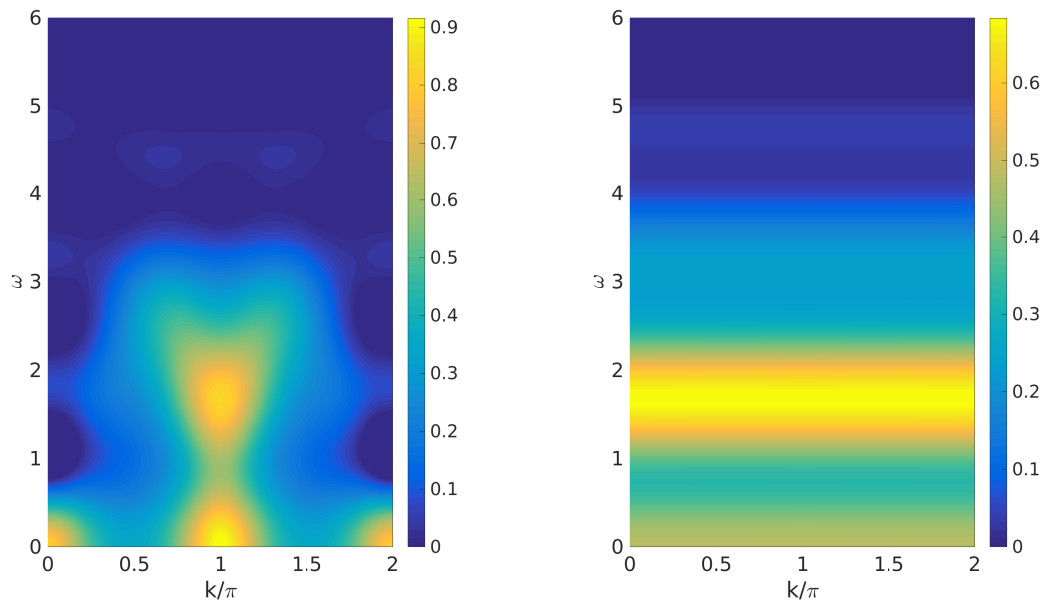**Figure 4.28:** $J_\perp = 1.38$, $J_\parallel = J_\times = 1$, $\beta = 1.5$, $T_{max} = 5.75\,s$

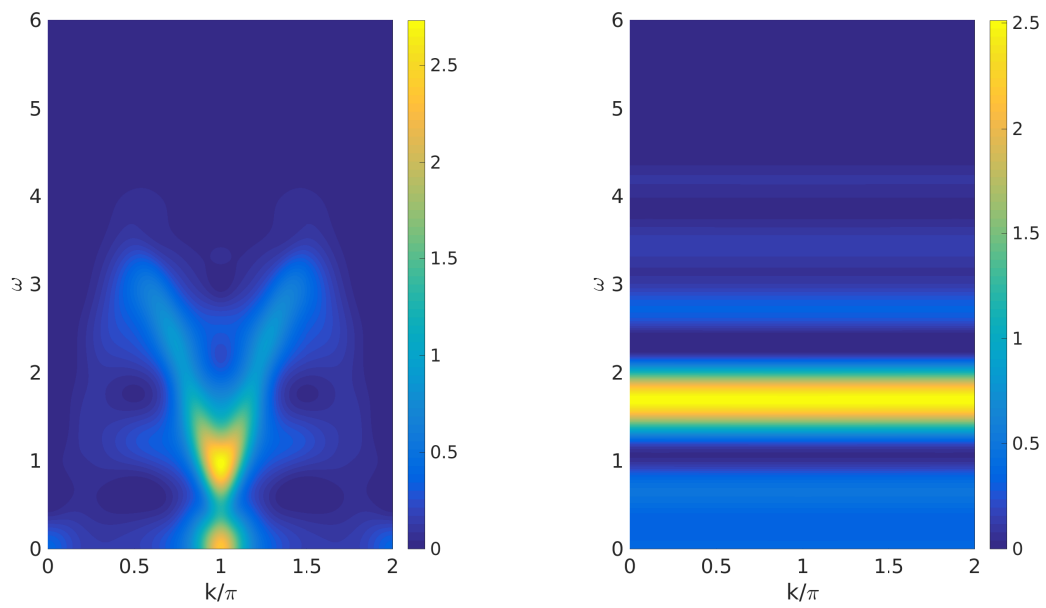**Figure 4.29:** $J_\perp = 1.38$, $J_\parallel = J_\times = 1$, $\beta = 1$, $T_{max} = 4.85\,s$

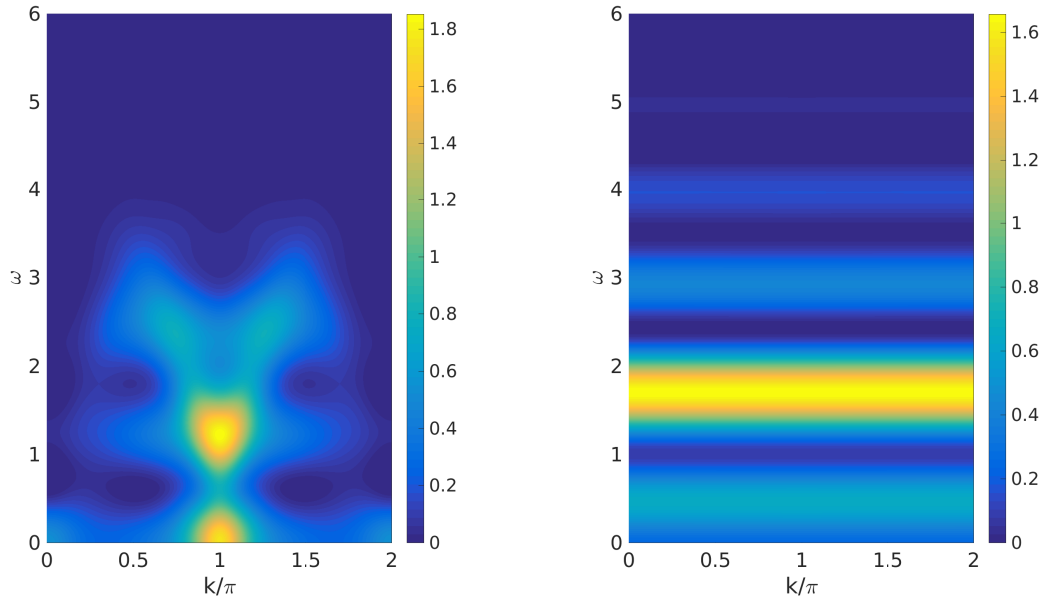**Figure 4.30:** $J_\perp = 1.41$, $J_\parallel = J_\times = 1$, $\beta = 3$, $T_{max} = 9.6\,s$

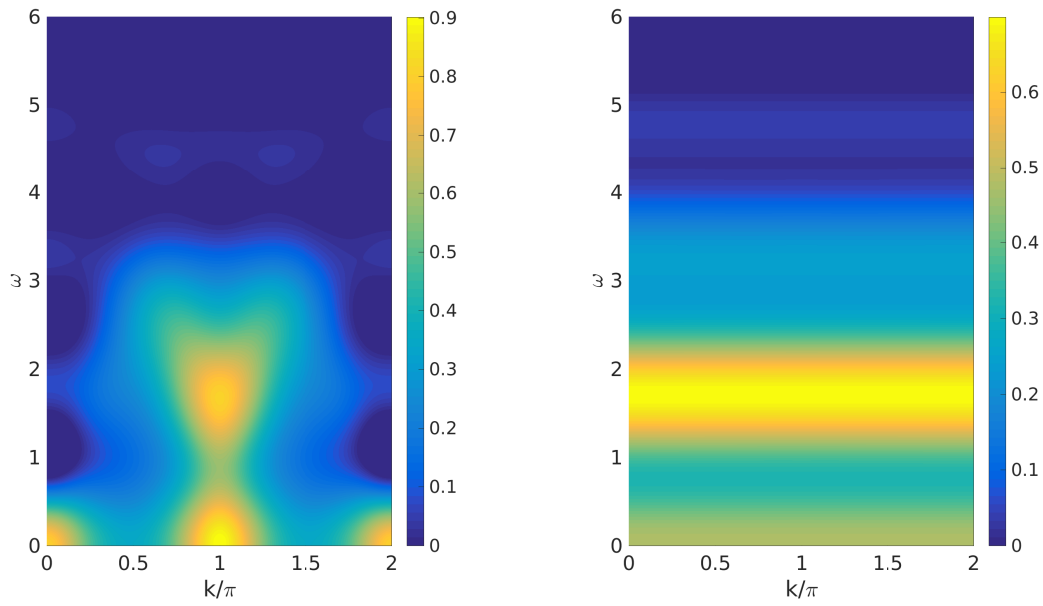**Figure 4.31:** $J_\perp = 1.41$, $J_\parallel = J_\times = 1$, $\beta = 2$, $T_{max} = 7.5\,s$

Figure 4.32: $J_\perp = 1.41$, $J_\parallel = J_\times = 1$, $\beta = 1$, $T_{max} = 5.1\,s$

If we compare the spectral weight of the first excited state in the vicinity of the phase transition (antisymmetric channel of Figs. 4.27-4.32) with parameter combinations away from criticality (antisymmetric channel of Figs. 4.18-4.20 and 4.21-4.26), we notice there is an accelerated redistribution taking place. Transitioning from $\beta = 3 \to 1$, for example, causes the spectral weight at $J_\perp = 1.41$ (Figs. 4.30-4.32) to drop by about 72%, while the same temperature jump causes the the a spectral weight drop $\approx 50\%$ at $J_\perp = 1.3$ (Figs. 4.18-4.20).

As mentioned before, this phenomenon can be understood by considering the presence of many non-dispersive excitations appearing in the vicinity of the phase transition. At $T = 0$, these excitations are not accessible because of selection rules in the spin-spin correlation function [15], but as we increase the temperature, thermal fluctuations allow us to access these levels too. When the temperature is of a magnitude comparable with the first excitation energy, we witness a continuum of excitations above the ground state level, meaning it is not protected by a gap anymore.

5. Conclusion

In this work, we have set out to inspect the interplay of quantum and thermal fluctuations on the spin-1/2 ladder with cross couplings using a tDMRG-based real-time evolution at zero and finite temperatures. In this way, we were able to access spectral data for system lengths of up at $L = 100$ for $T = 0$ calculations and $L = 50$ at finite temperatures, which go well beyond sizes accessible with exact diagonalization techniques. We were able to identify the two distinct phases of the ground state at $T = 0$ (rung-triplet and -singlet) and the closing of the spectral gap in the vicinity of the critical point. Bringing finite temperatures into play revealed the existence of non-dispersive modes below the first excitation in the antisymmetric channel. These modes are considered to cause the spectral weight redistribution onto the one-triplet excitation. As we approach the phase transition, an ever growing number of these non-dispersive modes fills the energetic gap in the antisymmetric channel, determining an accelerated spectral weight loss of the one triplet excitation. In the case of close vicinity to the phase transition, we witness an almost continuous spectral weight distribution above the ground state. The effects of geometrical frustration are inspected by comparing the spectra in the perfectly frustrated regime ($J_\times = J_\parallel = 1$, $J_{\perp,c} \approx 1.401$) with the spectra in a relaxed frustration regime ($J_\perp = J_\parallel = 1$, $J_{\times,c} \approx 0.599$). Comparing the dynamic structure factor reveals how perfect frustration yields completely localized excitations in the antisymmetric channel.

6. Appendices

6.1 Appendix A: the MPS algorithm

In the following, we will be looking into some of the technicalities regarding the transformation of a quantum state in MPS form.
The starting point is an arbitrary pure many body quantum state:

$$|\psi\rangle = \sum_{\sigma_1\cdots\sigma_L} \Psi_{\sigma_1\cdots\sigma_L} |\sigma_1\cdots\sigma_L\rangle, \, \sigma_i = 1,\cdots,d \; \forall i. \tag{6.1}$$

The multi-index object $\Psi_{\sigma_1\cdots\sigma_L}$ is what we want to bring in MPS form. We will proceed as follows: as a first step, we reshape the tensor $\Psi_{\sigma_1\cdots\sigma_L}$ into a $d \times (d^{L-1})$ object:

$$\Psi_{\sigma_1\cdots\sigma_L} = \Psi_{\sigma_1;(\sigma_2\cdots\sigma_L)}. \tag{6.2}$$

We then decompose the resulting matrix using singular value decomposition (SVD) [10, pp. 70-72]

$$\Psi_{\sigma_1;(\sigma_2\cdots\sigma_L)} = \sum_{a_1}^{r_1} U_{\sigma_1 a_1} S_{a_1 a_1} V^\dagger_{a_1;(\sigma_2\cdots\sigma_L)}. \tag{6.3}$$

We then introduce a simple change of notation:

$$U_{\sigma_1 a_1} \equiv A^{\sigma_1}_{a_1}, \tag{6.4}$$

$$S_{a_1 a_1} V^\dagger_{a_1;(\sigma_2\cdots\sigma_L)} \equiv \tilde{\Psi}_{a_1;(\sigma_2\cdots\sigma_L)}, \tag{6.5}$$

$$\Rightarrow \Psi_{\sigma_1\cdots\sigma_L} = \sum_{a_1}^{r_1} A^{\sigma_1}_{a_1} \tilde{\Psi}_{a_1;(\sigma_2\cdots\sigma_L)}. \tag{6.6}$$

At this point we reshape $\tilde{\Psi}_{a_1;(\sigma_2\cdots\sigma_L)}$ into $\tilde{\Psi}_{(a_1\sigma_2);(\sigma_3\cdots\sigma_L)}$ perform another SVD

$$\sum_{a_1}^{r_1} A^{\sigma_1}_{a_1} \tilde{\Psi}_{a_1;(\sigma_2\cdots\sigma_L)} = \sum_{a_1}^{r_1}\sum_{a_2}^{r_2} A^{\sigma_1}_{a_1} U_{(a_1\sigma_2);a_2} S_{a_2,a_2} V^\dagger_{a_2;(\sigma_3\cdots\sigma_L)}ß,. \tag{6.7}$$

Again, performing a notation change and reshaping in the last step we have:

$$U_{(a_1\sigma_2);a_2} \equiv A^{\sigma_2}_{a_1 a_2}, \tag{6.8}$$

$$S_{a_2,a_2} V^\dagger_{a_2;(\sigma_3\cdots\sigma_L)} \equiv \tilde{\tilde{\Psi}}_{a_2;(\sigma_3\cdots\sigma_L)} \rightarrow \tilde{\tilde{\Psi}}_{a_2\sigma_3;(\sigma_4\cdots\sigma_L)}, \tag{6.9}$$

$$\Psi_{\sigma_1\cdots\sigma_L} = \sum_{a_1}^{r_1}\sum_{a_2}^{r_2} A^{\sigma_1}_{a_1} A^{\sigma_2}_{a_1 a_2} \tilde{\tilde{\Psi}}_{a_2\sigma_3;(\sigma_4\cdots\sigma_L)}. \tag{6.10}$$

We can now again perform SVD on $\tilde{\tilde{\Psi}}_{a_2\sigma_3;(\sigma_4\cdots\sigma_L)}$ and continue adding A-Matrices for the entire length of the chain. The final result has the following form:

$$\Psi_{\sigma_1\cdots\sigma_L} = \sum_{a_1}^{r_1}\sum_{a_2}^{r_2}\cdots\sum_{a_{L-1}}^{r_{L-1}} A_{a_1}^{\sigma_1}A_{a_1a_2}^{\sigma_2}\cdots A_{a_{L-1}}^{\sigma_L}. \tag{6.11}$$

Plugging the final result in the initial wave equation we obtain:

$$|\psi\rangle = \sum_{\sigma_1\cdots\sigma_L}\left(\sum_{a_1}^{r_1}\sum_{a_2}^{r_2}\cdots\sum_{a_{L-1}}^{r_{L-1}} A_{a_1}^{\sigma_1}A_{a_1a_2}^{\sigma_2}\cdots A_{a_{L-1}}^{\sigma_L}\right)|\sigma_1\cdots\sigma_L\rangle. \tag{6.12}$$

For any configuration of $\{\sigma_i\}$, the expression between brackets represents the multiplication of a string of matrices $A^{\sigma_1}A^{\sigma_2}\cdots A^{\sigma_L}$

$$|\psi\rangle = \sum_{\sigma_1\cdots\sigma_L} A^{\sigma_1}A^{\sigma_2}\cdots A^{\sigma_L}|\sigma_1\cdots\sigma_L\rangle. \tag{6.13}$$

In pictorial language, the algorithm can be visualized as follows:
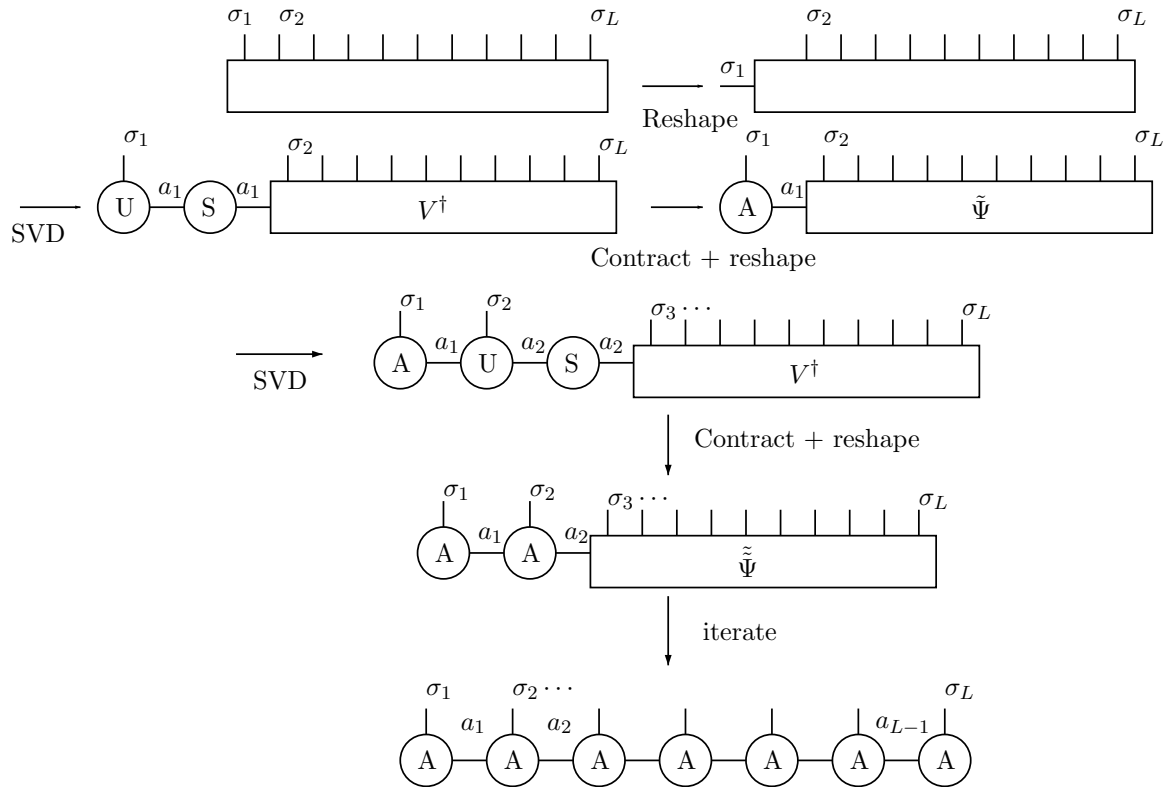

Figure 6.1: MPS algorithm in TN notation

The last expression is what we mean for MPS form of a pure state.

As a final remark, it should be noted how the A matrices inherit some of the convenient properties of the U matrices originating from SVD. It is known, that

$$U^\dagger U = \hat{I}. \tag{6.14}$$

A generic A matrix is related to the corresponding U matrix by the following:

$$A^{\sigma_i}_{a_{i-1},a_i} \equiv U_{a_{i-1}\sigma_i;a_i} \,, \tag{6.15}$$

with (14), we have:

$$\delta_{a_i,a_i'} = \sum_{a_{i-i}\sigma_i} U^\dagger_{a_i;a_{i-i}\sigma_i} U_{a_{i-i}\sigma_i;a_i'} \,, \tag{6.16}$$

$$\delta_{a_i,a_i'} = \sum_{a_{i-i}\sigma_i} A^{\sigma_i\dagger}_{a_i a_{i-i}} A^{\sigma_i}_{a_{i-i}a_i'} \,, \tag{6.17}$$

$$\Rightarrow \delta_{a_i,a_i'} = \sum_{\sigma_i} \left(A^{\sigma\dagger} A^\sigma \right)_{a_i a_i'} \,. \tag{6.18}$$

If the matrices of the MPS have the property (13), the MPS is said to be in left canonical form.

The last statement goes to show how MPS form of pure quantum state is not unique: we could have in fact started decomposing the initial Ψ tensor from the right. In that case, the resulting matrices end up having different properties [25, p. 24]. There are a number of different methods that yield slightly different properties of the matrices composing the MPS. What particular kind of MPS form should be used depend on the details of each application. For a complete overview of the different MPS forms we refer to Schollwoeck's review [25, pp. 18-24].

6.2   Appendix B: the Schmidt decomposition

In the following we will briefly discuss the Schmidt decomposition of a quantum state. Let us imagine a many body quantum state living in a composite Hilbert space $\mathcal{H}_{tot}$. In compact notation:

$$|\psi\rangle = \sum_{\sigma_1 \cdots \sigma_L} \Psi_{\sigma_1 \cdots \sigma_L} |\sigma_1 \cdots \sigma_L\rangle \,, |\sigma_1 \cdots \sigma_L\rangle \in \mathcal{H}_{tot} \,. \tag{6.19}$$

We now partition the Hilbert space in two and rewrite the wave equation of the resulting mixed state:

$$|\psi\rangle = \sum_{ij} \Psi_{ij} |i\rangle_A \otimes |j\rangle_B \text{ where } |i\rangle_A \in \mathcal{H}_A \,, |j\rangle_B \in \mathcal{H}_B \,, \tag{6.20}$$

$$\mathcal{H}_A \otimes \mathcal{H}_B = \mathcal{H}_{tot} \,. \tag{6.21}$$

We now perform SVD [10, pp. 70-72] on the tensor Ψ_{ij}:

$$|\psi\rangle = \sum_{ij} \sum_{a=1}^{min(N_A,N_B)} U_{ia} S_{aa} V^\dagger_{aj} |i\rangle_A \otimes |j\rangle_B \,. \tag{6.22}$$

The matrices U and $V^\dagger$ act separately on the subspaces $\mathcal{H}_A, \mathcal{H}_B$ and they induce a basis transformation but, since they result from a SVD, the orthonormality of the $|i\rangle_A \otimes |j\rangle_B$-basis remains preserved.

$$|\psi\rangle \;\; = \;\; \sum_{a=1}^{min(N_A,N_B)\equiv r} S_{aa} \left(\sum_i U_{ia} \, |i\rangle_A \right) \otimes \left(\sum_j V^\dagger_{aj} \, |j\rangle_B \right) , \tag{6.23}$$

$$|\psi\rangle \;\; = \;\; \sum_{a=1}^{r} S_a \, |a\rangle_A \otimes |a\rangle_B . \tag{6.24}$$

The advantage provided by this new representation is the resulting diagonal representation of the reduced density operators on the two subspaces:

$$\hat{\rho}_{\{A,B\}} = Tr_{\{B,A\}} (|\Psi\rangle \, \langle\Psi|) \;\; = \;\; \sum_{a=1}^{r} s_a^2 \, |a\rangle_{\{A,B\}} \, \langle a|_{\{A,B\}} . \tag{6.25}$$

Loosely speaking, the Schmidt decomposition amounts to nothing more than transforming the basis vectors composing an arbitrary quantum state in a new basis in which the density matrix is diagonal.

Acknowledgments

Bibliography

[1] Jason Alicea, Andrey V. Chubukov, and Oleg A. Starykh. "Quantum stabilization of 1/3-magnetization plateau in Cs_2CuBr_4". In: *Phys. Rev. Lett. 102, 137201 (2009)* (Sept. 22, 2008). DOI: 10.1103/PhysRevLett.102.137201. arXiv: 0809.3800v1 [cond-mat.str-el].

[2] Neil W. Ashcroft and N. Mermin. *Solid State Physics*. Cengage Learning, Inc, Jan. 2, 1976. 848 pp. ISBN: 0030839939. URL: http://www.ebook.de/de/product/3237015/neil_w_ashcroft_n_mermin_solid_state_physics.html.

[3] Pierre Bouillot et al. "Statics and dynamics of weakly coupled antiferromagnetic spin-1/2 ladders in a magnetic field". In: *Phys. Rev. B 83, 054407 (2011)* (Sept. 4, 2010). DOI: 10.1103/PhysRevB.83.054407. arXiv: 1009.0840v2 [cond-mat.str-el].

[4] A V Chubokov and D I Golosov. "Quantum theory of an antiferromagnet on a triangular lattice in a magnetic field". In: *Journal of Physics: Condensed Matter* 3.1 (1991), p. 69. URL: http://stacks.iop.org/0953-8984/3/i=1/a=005.

[5] A V Chubukov, S Sachdev, and T Senthil. "Large-S expansion for quantum antiferromagnets on a triangular lattice". In: *Journal of Physics: Condensed Matter* 6.42 (1994), p. 8891. URL: http://stacks.iop.org/0953-8984/6/i=42/a=019.

[6] A. J. Daley et al. "Time-dependent density-matrix renormalization-group using adaptive effective Hilbert spaces". In: *J. Stat. Mech.: Theor. Exp. (2004) P04005* (Mar. 12, 2004). DOI: 10.1088/1742-5468/2004/04/P04005. arXiv: cond-mat/0403313v2 [cond-mat.str-el].

[7] H.T. Diep. *Frustrated Spin Systems*. World Scientific Publishing Company, 2013. ISBN: 9789814440752. URL: https://books.google.de/books?id=HP-6CgAAQBAJ.

[8] J. Eisert, M. Cramer, and M. B. Plenio. "Area laws for the entanglement entropy - a review". In: *Rev. Mod. Phys. 82, 277 (2010)* (Aug. 28, 2008). DOI: 10.1103/RevModPhys.82.277. arXiv: 0808.3773v4 [quant-ph].

[9] Martin P. Gelfand. "Linked-tetrahedra spin chain: Exact ground state and excitations". In: *Phys. Rev. B* 43 (10 Apr. 1991), pp. 8644–8645. DOI: 10.1103/PhysRevB.43.8644. URL: https://link.aps.org/doi/10.1103/PhysRevB.43.8644.

[10] Charles F. Golub Gene H. Van Loan. *Matrix Computations. Third Edition*. The Johns Hopkins University Press, 1996. ISBN: 0-8018-5414-8. URL: https://www.amazon.com/Matrix-Computations-Third-Charles-Golub/dp/B007CV78PU?SubscriptionId=0JYN1NVW651KCA56C102&tag=techkie-20&linkCode=xm2&camp=2025&creative=165953&creativeASIN=B007CV78PU.

[11] M. B. Hastings. "An Area Law for One Dimensional Quantum Systems". In: *JSTAT, P08024 (2007)* (May 14, 2007). DOI: 10.1088/1742-5468/2007/08/P08024. arXiv: 0705.2024v3 [quant-ph].

[12] Naomichi Hatano and Masuo Suzuki. "Finding Exponential Product Formulas of Higher Orders". In: *"Quantum Annealing and Other Optimization Methods," Eds. A. Das and B.K. Chakrabarti (Springer, Berlin, 2005) pp. 37-68* (June 2, 2005). DOI: `10.1007/11526216_2`. arXiv: `math-ph/0506007v1 [math-ph]`.

[13] Michael Hermele et al. "Properties of an algebraic spin liquid on the kagome lattice". In: *Phys. Rev. B 77, 224413 (2008)* (Mar. 7, 2008). DOI: `10.1103/PhysRevB.77.224413`. arXiv: `0803.1150v3 [cond-mat.str-el]`.

[14] A. Honecker, F. Mila, and M. Troyer. "Magnetization plateaux and jumps in a class of frustrated ladders: A simple route to a complex behaviour". In: *Eur. Phys. J. B15 (2000) 227-233* (Oct. 27, 1999). DOI: `10.1007/s100510051120`. arXiv: `cond-mat/9910438v2 [cond-mat.str-el]`.

[15] Andreas Honecker, Frédéric Mila, and B. Normand. "Multi-triplet bound states and finite-temperature dynamics in highly frustrated quantum spin ladders". In: *Phys. Rev. B 94, 094402 (2016)* (May 30, 2016). DOI: `10.1103/PhysRevB.94.094402`. arXiv: `1605.09392v2 [cond-mat.str-el]`.

[16] A. Honecker et al. "Thermodynamic properties of highly frustrated quantum spin ladders: Influence of many-particle bound states". In: *Phys. Rev. B* 93 (5 Feb. 2016), p. 054408. DOI: `10.1103/PhysRevB.93.054408`. URL: `https://link.aps.org/doi/10.1103/PhysRevB.93.054408`.

[17] H. Kageyama et al. "Direct Evidence for the Localized Single-Triplet Excitations and the Dispersive Multitriplet Excitations in $SrCu_2(BO_3)_2$". In: *Phys. Rev. Lett.* 84 (25 June 2000), pp. 5876–5879. DOI: `10.1103/PhysRevLett.84.5876`. URL: `https://link.aps.org/doi/10.1103/PhysRevLett.84.5876`.

[18] Erik Koch. "8 The Lanczos Method". In: *The LDA+ DMFT approach to strongly correlated materials* (2011).

[19] C. Lacroix, P. Mendels, and F. Mila. *Introduction to Frustrated Magnetism: Materials, Experiments, Theory*. Springer Series in Solid-State Sciences. Springer Berlin Heidelberg, 2011. ISBN: 9783642105890. URL: `https://books.google.de/books?id=utSV09ZuhOkC`.

[20] Andreas M. Läuchli, Julien Sudan, and Roderich Moessner. "The $S = 1/2$ Kagome Heisenberg Antiferromagnet Revisited". In: (Nov. 21, 2016). arXiv: `1611.06990v1 [cond-mat.str-el]`.

[21] Reinhard M. Noack. "Diagonalization- and Numerical Renormalization-Group-Based Methods for Interacting Quantum Systems". In: *AIP Conference Proceedings*. AIP, 2005. DOI: `10.1063/1.2080349`.

[22] Roman Orus. "A Practical Introduction to Tensor Networks: Matrix Product States and Projected Entangled Pair States". In: *Annals of Physics 349 (2014) 117-158* (June 10, 2013). DOI: `10.1016/j.aop.2014.06.013`. arXiv: `1306.2164v3 [cond-mat.str-el]`.

[23] B.Sutherland S. Shastry. "Exact Ground State of a Quantum-Mechanical Antiferromagnet". In: *Physica 108B, 1069 (1981)* (1981). URL: `http://physics.ucsc.edu/~sriram/papers/paper_19.pdf`.

[24] Subir Sachdev. *Quantum Phase Transitions*. Cambridge University Press, 2011. ISBN: 978-0-521-51468-2. URL: `https://www.amazon.com/Quantum-Phase-Transitions-Subir-Sachdev-ebook/dp/B00AKE1YE2?SubscriptionId=0JYN1NVW651KCA56C102&tag=techkie-20&linkCode=xm2&camp=2025&creative=165953&creativeASIN=B00AKE1YE2`.

[25] Ulrich Schollwoeck. "The density-matrix renormalization group in the age of matrix product states". In: *Annals of Physics 326, 96 (2011)* (Aug. 20, 2010). DOI: 10.1016/j.aop.2010.09.012. arXiv: 1008.3477v2 [cond-mat.str-el].

[26] G.L. Squires. *Introduction to the Theory of Thermal Neutron Scattering.* Dover books on physics. Dover Publications, 1978. ISBN: 9780486694474. URL: https://books.google.de/books?id=Lx4xcz3v9IMC.

[27] E M Stoudenmire and Steven R White. "Minimally entangled typical thermal state algorithms". In: *New Journal of Physics* 12.5 (2010), p. 055026. URL: http://stacks.iop.org/1367-2630/12/i=5/a=055026.

[28] F. Verstraete, J. J. Garcia-Ripoll, and J. I. Cirac. "Matrix Product Density Operators: Simulation of finite-T and dissipative systems". In: *Phys. Rev. Lett. 93, 207204 (2004)* (June 18, 2004). DOI: 10.1103/PhysRevLett.93.207204. arXiv: cond-mat/0406426v2 [cond-mat.other].

[29] G. Vidal. "Efficient simulation of one-dimensional quantum many-body systems". In: *Phys. Rev. Lett. 93, 040502 (2004)* (Oct. 14, 2003). DOI: 10.1103/PhysRevLett.93.040502. arXiv: quant-ph/0310089v1 [quant-ph].

[30] Stefan Wessel et al. "Efficient Quantum Monte Carlo simulations of highly frustrated magnets: the frustrated spin-1/2 ladder". In: (Apr. 6, 2017). arXiv: 1704.01973v1 [cond-mat.str-el].

[31] Steven R. White. "Density matrix formulation for quantum renormalization groups". In: *Phys. Rev. Lett.* 69.19 (Nov. 1992), pp. 2863–2866. DOI: 10.1103/PhysRevLett.69.2863.

[32] Steven R. White. "Density matrix renormalization group algorithms with a single center site". In: (Aug. 29, 2005). DOI: 10.1103/PhysRevB.72.180403. arXiv: cond-mat/0508709v1 [cond-mat.str-el].

[33] Steven R. White and Adrian E. Feiguin. "Real time evolution using the density matrix renormalization group". In: *Phys. Rev. Lett. 93, 076401 (2004)* (Mar. 12, 2004). DOI: 10.1103/PhysRevLett.93.076401. arXiv: cond-mat/0403310v2 [cond-mat.str-el].

[34] Steven R. White and David A. Huse. "Numerical renormalization-group study of low-lying eigenstates of the antiferromagnetic S=1 Heisenberg chain". In: *Phys. Rev. B* 48 (6 Aug. 1993), pp. 3844–3852. DOI: 10.1103/PhysRevB.48.3844. URL: https://link.aps.org/doi/10.1103/PhysRevB.48.3844.

[35] Y. Xian. "Rigorous results on a first-order phase transition in antiferromagnetic spin-1/2 coupled chains". In: *Phys. Rev. B* 52 (17 Nov. 1995), pp. 12485–12488. DOI: 10.1103/PhysRevB.52.12485. URL: https://link.aps.org/doi/10.1103/PhysRevB.52.12485.

[36] I. A. Zaliznyak, S. -H. Lee, and S. V. Petrov. "Continuum in the spin excitation spectrum of a Haldane chain, observed by neutron scattering in CsNiCl3". In: *Phys. Rev. Lett. 87, 017202 (2001)* (Oct. 3, 2000). DOI: 10.1103/PhysRevLett.87.017202. arXiv: cond-mat/0010049v1 [cond-mat.str-el].

[37] Chen Zeng and Veit Elser. "Quantum dimer calculations on the spin-1/2 kagomé Heisenberg antiferromagnet". In: *Phys. Rev. B* 51 (13 Apr. 1995), pp. 8318–8324. DOI: 10.1103/PhysRevB.51.8318. URL: https://link.aps.org/doi/10.1103/PhysRevB.51.8318.

Selbstständigkeitserklärung

Hiermit erkläre ich, die vorliegende Arbeit selbständig verfasst zu haben und keine anderen als die in der Arbeit angegebenen Quellen und Hilfsmittel benutzt zu haben.

München, den 6. August 2017